

RESEARCH

Open Access

# Self-adaptive algorithm for segmenting skin regions

Michał Kawulok\*, Jolanta Kawulok, Jakub Nalepa and Bogdan Smolka

## Abstract

In this paper, we introduce a new self-adaptive algorithm for segmenting human skin regions in color images. Skin detection and segmentation is an active research topic, and many solutions have been proposed so far, especially concerning skin tone modeling in various color spaces. Such models are used for pixel-based classification, but its accuracy is limited due to high variance and low specificity of human skin color. In many works, skin model adaptation and spatial analysis were reported to improve the final segmentation outcome; however, little attention has been paid so far to the possibilities of combining these two improvement directions. Our contribution lies in learning a local skin color model on the fly, which is subsequently applied to the image to determine the seeds for the spatial analysis. Furthermore, we also take advantage of textural features for computing local propagation costs that are used in the distance transform. The results of an extensive experimental study confirmed that the new method is highly competitive, especially for extracting the hand regions in color images.

**Keywords:** Skin detection; Skin segmentation; Adaptive color model; Spatial analysis

## 1 Introduction

Detection and segmentation of human skin regions [1,2] in color images is an active research topic, which receives considerable attention from image and signal processing community. Skin detection consists in taking a binary decision whether an image, its region, or a particular pixel presents the human skin. In case of the positive answer, skin segmentation is applied to determine the exact boundaries of the detected skin regions. Applications of skin detection and segmentation are of a wide range and significance, and they include gesture recognition for human-computer interaction [3], objectionable content filtering [4], content-based image retrieval [5], medical imaging [6,7], and image coding [8].

### 1.1 Overview of skin detection and segmentation techniques

The existing methods are based on the premise that the skin color can be effectively modeled in various color spaces, which allows segmenting the skin regions in color images. Using skin color models, every pixel may be classified to the skin or non-skin class based on its

position in the color space, independently from its neighbors. Alternatively, the probability that each pixel presents the skin can be determined, which transforms a color image into a *skin probability map* ( $P_S$ ). The map may be binarized using a certain acceptance threshold in order to extract the skin regions. This problem has been widely studied, and a large number of skin color models were introduced over the years. The main difference between them lies in their learning and generalization capabilities, but given a sufficiently large training set, their effectiveness is similar, and it is limited due to high variance and low specificity of human skin color [2]. Basically, skin and non-skin pixels overlap in color spaces; hence, they cannot be separated relying exclusively on their color. The pixel-wise classification may be improved by incorporating information extracted from the texture, as well as by spatial analysis of the pixels that have high skin probability. Also, global skin color models may be adapted to a particular scene or an individual who appears in the image, which improves the classification accuracy, providing that the adaptation is correct.

### 1.2 Contribution

In the work reported here, we introduce a new method that consists in combining three important elements,

\*Correspondence: michał.kawulok@polsl.pl

Faculty of Automatic Control, Electronics and Computer Science, Silesian University of Technology, Akademicka 16, 44-100 Gliwice, Poland

namely, (i) skin color model adaptation, (ii) spatial analysis, and (iii) exploitation of the textural features. First, a skin probability map is obtained from the input image using a global model. The map is processed to extract skin samples, used to create a local skin color model. Subsequently, the local model is applied to locate the seeds for spatial analysis, which determines the final boundaries of the skin regions. We perform the spatial analysis using the *discriminative skin-presence features* (DSPF), introduced in our earlier work [9], that rely on textural properties of skin probability maps.

There have been a handful of methods proposed [10,11] that combine model adaptivity with spatial analysis. These techniques require a skin sample for the adaptation, delivered by a face detector, and they do not exploit textural features. Naturally, these methods cannot perform the adaptation when a face is not visible or if a face detector fails.

In the proposed approach, the model is adapted based on analysis of a skin probability map, without using any additional information sources. The reported experimental results clearly show that our algorithm achieves better segmentation scores than alternative state-of-the-art methods. Furthermore, the new method significantly increases the detection precision, which is particularly important when a hand region is to be segmented for the hand pose estimation purposes.

### 1.3 Paper structure

The paper is organized as follows. In Section 2, the existing approaches to skin detection and segmentation are outlined, with particular attention given to the adaptation techniques. Spatial analysis methods used in our study are described in Section 3, and the proposed skin detection algorithm is presented in details in Section 4. Experimental validation is reported and discussed in Section 5. Section 6 concludes our study. Furthermore, the symbols used in the paper are explained in Table 1.

## 2 Related literature

Skin detection and segmentation has been widely studied over the last 20 years, and a lot of advancements emerged so far. A large number of contributions address the problem of skin color modeling in various color spaces, and they are well summarized in a survey published in 2007 by Kakumanu et al. [1].

Skin color can be modeled using a set of rules and thresholds defined in color spaces based on some observations [12-15]. Alternatively, given a representative training set, skin detection rules can be determined using machine learning. Jones and Rehg [16] proposed to train the Bayesian classifier in the RGB space. This requires a training set containing pixels assigned to the skin ( $\mathcal{C}_s$ ) and non-skin ( $\mathcal{C}_{ns}$ ) classes. Color histograms are built for these

**Table 1 The symbols used in the paper**

Symbol	Description
General symbols	
$\mathcal{I}$	Input color image
$\mathcal{C}_s$	Skin class
$\mathcal{C}_{ns}$	Non-skin class
$P$	Probability
$\mathcal{P}_S$	Skin probability map
$\mathcal{H}$	Histogram
$\Sigma$	Covariance matrix
$\mathcal{B}$	A set of blobs
$\mathcal{N}_{n \times n}(x)$	A set of pixels in the $n \times n$ kernel around the pixel $x$
$\delta_{fp}$	False-positive rate
$\delta_{min}$	Minimal error
Symbols related with the DT-based spatial analysis (including the DSPF space)	
$\Gamma$	Total path cost
$\gamma$	Overall local cost
$\gamma_p$	Destination-probability local cost component
$\gamma_\Delta$	Local cost component related with the difference in the propagation domain
$\mathcal{T}_\alpha^P$	High-probability seed extraction threshold
$\mathcal{T}_\beta^P$	Lower-bound propagation threshold
$\mathcal{T}_0^P$	Costless propagation threshold
$\mathcal{T}_T^P$	Total path cost threshold
$D$	Distance in the DSPF space
$v$	Feature vector in the DSPF space
$r$	Reference pixel
$P_r$	Reference skin probability (determined in the neighborhood of $r$ )
Symbols related with the self-adaptive seeds method	
$\mathcal{S}^0$	Initial skin seeds
$\mathcal{S}^E$	Expanded skin seeds
$\mathcal{S}^A$	Adapted (final) skin seeds
$t_{seed}$	Dynamic initial binarization threshold
$\mathcal{R}_{seed}$	Ratio of pixels used to determine $t_{seed}$
$\mathcal{T}_A^P$	Binarization threshold used to extract $\mathcal{S}^A$ from the local skin probability map
$\mathcal{T}_{seed}^P$	Minimum acceptable value of $t_{seed}$
$\mathcal{T}_r^P$	Threshold for the reference skin probability (in the dilated $\mathcal{P}_S$ )
$\gamma_\Delta^E$	Local difference costs ( $\gamma_\Delta$ ) used for building the expanded
$\gamma_\Delta^F$	Local difference costs ( $\gamma_\Delta$ ) used for final 'skinniness' propagation

two classes:  $P(v|\mathcal{C}_s)$  and  $P(v|\mathcal{C}_{ns})$ , where  $v$  is the color, and the probability that a given pixel presents the skin (i.e.,  $P(\mathcal{C}_s|v)$ ) is determined from the Bayes rule. This is a robust approach, provided that a sufficiently large training set is available. In the majority of cases, it is beneficial to reduce the number of histogram bins per channel to increase the generalization capacity [2,17]. Analysis of color histograms has also been applied to solve more general tasks concerning extracting image regions [18].

Greenspan et al. [19] used Gaussian mixture models (GMMs) for learning human skin color in the normalized  $rg$  chromaticity space. GMMs offer better generalization capabilities than the Bayesian classifier, and they were later exploited in many approaches to skin color modeling [20,21]. In our recent survey [2], we demonstrated that GMMs outperform the Bayesian classifier for small training sets; however, for larger sets, the latter was more accurate.

Among other machine learning techniques applied to skin detection, it is worth to mention artificial neural networks (ANNs) [22,23], support vector machines [24,25], and random forests [10]. In general, the methods based on machine learning achieve higher classification accuracy than the rule-based approaches.

Skin detection and segmentation plays also an important role in dermoscopy for skin lesions segmentation and analysis. This is an active research topic of medical imaging, and many methods have been developed over time [6]. Segmentation of skin lesions may be performed using a number of techniques, which take advantage of the skin homogeneity in the domain of color, luminance or texture, and they include statistical region merging [26,27], dynamic programming [28], and wavelet-based texture analysis [7]. The segmentation phase is followed by shape analysis to investigate the lesion type [29]. In general, these methods are specialized to deal with the dermoscopy images. It is therefore assumed that a given image presents human skin with some lesions that should be segmented from the background.

## 2.1 Adaptive skin color modeling

Accuracy of skin detection using color models is limited due to the overlapping between skin and non-skin pixels, which may be observed in various color spaces. If the model is created so that it omits the overlapping values, then many skin pixels are classified as background, decreasing the recall. On the other hand, if the model includes these overlapping values, then the number of false-positives (FP) is increased. It is worth noting that the overlap may be reduced, if a skin model is adapted to individuals who appear in a presented scene. Given constant lighting conditions and a limited number of individuals in the image, skin color specificity is definitely higher than in

the general case, and overall, the skin regions can be better separated from the background.

Basically, the existing adaptation methods either require a skin sample, from which the local skin model is learned on the fly, or they use some features extracted from an input image to fit the model. In the latter case, several approaches exploit ANNs for the adaptation. Lee et al. [4] used a multilayer perceptron to select the most appropriate skin model from a collection of models, each of which was trained earlier for specific lighting conditions. ANNs were also used to tune the parameters of the Gaussian intended to model the skin color, given an image histogram [30], as well as to determine an optimal acceptance threshold [31] for each skin probability map obtained using a global model. Sun [32] applied a global skin model to extract skin pixels, whose distribution was subsequently modeled using GMM. Final skin probability was determined relying on that locally learned GMM combined with the global model. In this way, those pixels preliminarily classified as skin, which do not form clusters in the color space, are reclassified as background.

Skin models can also be effectively adapted given a skin sample, acquired based on tracking skin-like objects in video sequences [33], or relying on face [11,34] or hand [3] detection. For such a skin sample, a local model can be generated using the Bayesian classifier [35,36] or GMMs [37] as they do not require time-consuming training. However, although the local model allows detecting the skin with high precision, the recall is often low. To address this problem, the local model is combined with the global one. The final probability  $P_f(\mathcal{C}_s|v)$  can be computed as a weighted mean of the probabilities obtained using the local  $P_l(\mathcal{C}_s|v)$  and global  $P_g(\mathcal{C}_s|v)$  models.

Another approach adopted here consists in using a global skin color locus, which imposes a restriction on the adaptation [37,38]. It is also possible to combine the local and global models by incorporating them into a spatial analysis framework, which is given more attention later in this section.

Alternatively, a skin sample may be used to optimize the value of the acceptance thresholds [3,39]. Recently, Yogarajah et al. [40] proposed to use skin samples for adapting the acceptance thresholds in a single-dimensional error signal space (ESS) [14]. ESS is obtained from RGB, and skin color can be modeled here using a single Gaussian.

The Yogarajah's method consists in analyzing the distribution of the error signal in a facial region to determine the decision thresholds from the obtained Gaussian parameters.

## 2.2 Textural and spatial analysis

Although the color-based skin models can be adapted to a given image, which reduces the false-positives, Zhu et al.

[41] demonstrated that even for perfect adaptation, in most situations, the skin cannot be completely separated from the background in a given color space. The discriminative power of skin classifiers may be increased, when the pixels neighborhood is taken into account, for example, exploiting textural features extracted from an input image.

Wang et al. [42] proposed to enhance the segmentation in the RGB and YCgCb color spaces by analyzing various textural features, extracted using the gray-level co-occurrence matrix. Moreover, simple textural features were used to boost the performance of a number of skin detection techniques and classifiers, including the ANNs [43], non-parametric density estimation of skin and non-skin classes [44], GMMs [45], and many more [46–49]. In our earlier work [50], we found it beneficial to extract textural features from skin probability maps rather than from the input images.

Skin detection accuracy may also be increased using the region-growth operations, because skin pixels are usually grouped, whereas the non-skin false-positives are scattered in the spatial domain. Here, conventional image segmentation algorithms can be applied, for example, those based on combined Markov random fields [51], or probabilistic bottom-up aggregation [52]. It may be beneficial to extract and utilize some textural features, for example, using wavelets [7,53]. Although this is a time-consuming technique, it has been demonstrated that it may be successfully optimized for DSP processors [54]. Overall, a number of specific methods devoted to segmenting skin regions have been developed. Kruppa et al. [5] proposed to verify the potential skin regions assuming that they should have an elliptical shape. In other works, a threshold hysteresis in skin probability maps was applied to accept those regions, which are connected with the seeds of high skin probability [36,55]. Furthermore, spatial properties of skin regions were analyzed using conditional random fields [56] and cellular automata [49]. Del Solar and Verschae proposed to analyze skin probability maps using controlled diffusion [57]. At first, the diffusion seeds are formed by those pixels, whose skin probability exceeds the *seed threshold* ( $T_\alpha^P$ ). Then, the neighboring pixels are iteratively adjoined to the skin region, if they meet the diffusion process criteria, provided that their skin probability is larger than the *lower-bound propagation threshold* ( $T_\beta^P$ ).

In our earlier research [58], we introduced an energy-based technique for skin blobs analysis. The skin regions are expanded depending on the amount of energy, which is spread over the image, according to the local skin probability. Recently, we proposed to use the distance transform (DT) in a combined domain of hue, luminance, and skin probability [59,60]. Furthermore, we elaborated on the importance of seeds detection, from which the skin probability (termed ‘skinness’) is propagated. This method

is exploited in the research reported here, and it is given more attention in Section 3.

### 2.3 Hybrid methods

There are relatively few methods that combine the aforementioned improvement strategies, and the research reported in this paper also falls into this category.

Jiang et al. [61] proposed to take advantage of color, texture, and space analysis. At first, the skin regions are determined based on a skin probability map obtained from color information. Subsequently, the regions are refined to improve the precision, relying on the textural features extracted using the Gabor wavelets. Finally, the regions are grown with the watershed segmentation to exploit the spatial information.

Combining textural features with spatial analysis was also the key contribution of our recent work [9]. We introduced the DSPF space, which is exploited to compute the local costs for DT, instead of using the skin probability map as in [59]. As we also use the DSPF domain in our study, this method is given more attention in Section 3.

In our another work [11], we explored how to combine a local skin color model with the global one using spatial analysis. We applied the face-based local model to detect the skin seeds, from which the ‘skinniness’ is propagated using DT to adjoin the skin pixels. A similar approach was proposed by Khan et al. [62], where the local model is learned from the facial region. The model is used to obtain the foreground weights for the graph-cut image segmentation, and the background weights are obtained using the global skin color model. A potential drawback of this method lies in using a generic image segmentation algorithm, whose parameters are difficult to tune. Unfortunately, the implementation is not available, and the paper does not include all the details necessary to reproduce the results. The method was validated using thousands of video frames. Although this is a huge data set, the number of scenes and individuals is quite small, as the images were extracted from only 25 videos and the conditions within each single video are uniform. Also, the authors claim to have used 8,991 images for validation, while the entire data set contains 10,764 frames, and it is unclear which images were excluded. Last, but not least, the method is quite slow, as it requires 1.5 s to process a small  $100 \times 100$  image.

## 3 Distance transform for spatial analysis

In the research reported here, we adopted the spatial analysis framework, developed during our earlier study [59]. The method consists of two general phases, namely, (i) seeds extraction and (ii) propagation from the seeds using DT. These phases are described in this section, along with the texture analysis technique [9], which additionally improves the results obtained using DT.

### 3.1 Propagation seeds

The aim of the seeds extraction is to determine the initial skin regions, from which the ‘skinniness’ is propagated. The seeds are considered as skin, and neighboring pixels are subsequently adjoined to the skin region using DT. In an ideal case, not only should the seeds contain no false-positive pixels but also every ground-truth skin blob (i.e., a region composed of the real skin pixels) should include at least one detected seed inside. Otherwise, such a region would not be adjoined to the skin class during the propagation, increasing the false-negative (FN) rate.

The seeds can be extracted taking advantage of the observation that if the skin probability map is binarized using a high-probability threshold, then the precision is rather high, because usually only true-positive (TP) skin regions contain pixels with very high skin probability values. If the skin probability of an individual pixel is over a high threshold  $\mathcal{T}_\alpha^P$ , then the pixel is added to the seed. Such an approach was adopted in many spatial analysis methods [36,55,57].

Recently, we proposed to create an adaptive seed based on detected facial regions [11]. Using the geometrical features extracted from the luminance channel of the input color image, the facial regions are detected. A local skin model is learned using a single multivariate Gaussian, and the model is applied to the input image to obtain a local skin probability map, which is binarized to determine the final seeds. Afterwards, the propagation is carried out using the skin probability map obtained from a global skin color model.

### 3.2 ‘Skinness’ propagation

In order to propagate the ‘skinniness’ from the seeds, the shortest routes from the seed to every pixel are determined at first. This is achieved by minimizing *total path costs* from the set of seed pixels to each non-seed pixel in the image. The total path cost for a pixel  $x$  is defined as

$$\Gamma(x) = \sum_{i=0}^{l-1} \gamma(p_i \rightarrow p_{i+1}), \quad (1)$$

where  $\gamma$  is a local propagation cost between two neighboring pixels,  $p_0$  is a pixel that lies at the seed boundary,  $p_l = x$ , and  $l$  is the total path length. The minimization is performed using the Dijkstra’s algorithm [63]. In addition, the threshold  $\mathcal{T}_\beta^P = 0.3$  is used as proposed in [57], which prevents propagating to the regions of very low skin probability. Furthermore, mainly to decrease the execution time, the propagation is terminated if the total path cost exceeds a certain boundary value  $\mathcal{T}_\Gamma$ .

The route optimization outcome heavily depends on how the local costs  $\gamma$  are computed. For skin segmentation, we construct the local cost using two major components, namely the difference in the propagation domain

$\gamma_\Delta$  and the destination-probability cost  $\gamma_p$ . The local cost from a pixel  $x$  to  $y$ , i.e.,  $\gamma(x \rightarrow y)$  is obtained as

$$\gamma(x \rightarrow y) = \gamma_\Delta(x, y) \cdot [1 + \gamma_p(x \rightarrow y)], \quad (2)$$

where

$$\gamma_p(x \rightarrow y) = \begin{cases} -1 & \text{for } P(y) > \mathcal{T}_0^P \\ 1 - P(y) & \text{for } \mathcal{T}_\beta^P < P(y) \leq \mathcal{T}_0^P \\ \infty & \text{for } P(y) \leq \mathcal{T}_\beta^P \end{cases}. \quad (3)$$

$P(y)$  is the skin probability of the pixel  $y$  and  $\mathcal{T}_0^P$  is the costless propagation threshold (if the skin probability at pixel  $y$  exceeds  $\mathcal{T}_0^P$ , then the total path cost does not increase when moving from pixel  $x$  to  $y$ ). The difference cost  $\gamma_\Delta$  was originally defined using hue and luminance values:

$$\gamma_\Delta(x, y) = \alpha_d \cdot (|Y(x) - Y(y)| + |H(x) - H(y)|), \quad (4)$$

where  $\alpha_d \in \{1, \sqrt{2}\}$  is the penalty for propagation in the diagonal direction,  $Y(\cdot)$  is the pixel luminance, and  $H(\cdot)$  is the hue in the HSV color model, both scaled to the range from 0 to 255.

The total path cost obtained after the optimization is inversely proportional to the ‘skinniness’; hence, the final skin probability map is obtained by scaling the costs from 0 (for the maximal cost) to 1 (for a zero cost, i.e., the seed pixels). The pixels not adjoined during the propagation process (i.e., those whose total path cost  $\Gamma$  is greater than  $\mathcal{T}_\Gamma$ ) are assigned with zeroes. Finally, the skin regions are extracted using a fixed threshold in the distance domain.

In the research reported in this paper, we consider alternative local difference costs (explained below), which we found effective in various ‘skinniness’ propagation scenarios.

1. Restrictive hue-luminance difference cost:

$$\gamma_\Delta^{(HL)}(x, y) = \alpha_d \cdot \max(|Y(x) - Y(y)|, |H(x) - H(y)|). \quad (5)$$

2. Cost based on a difference in the RGB color space:

$$\gamma_\Delta^{(RGB)}(x, y) = \alpha_d \cdot (|R(x) - R(y)| + |G(x) - G(y)| + |B(x) - B(y)|). \quad (6)$$

3. Skin probability difference cost:

$$\gamma_\Delta^{(SP)}(x, y) = \alpha_d \cdot |\mathcal{P}_S(x) - \mathcal{P}_S(y)|. \quad (7)$$

### 3.3 Discriminative skin-presence features domain

For computing the destination-probability cost  $\gamma_p$ , the skin probability map obtained with the global skin model was originally used [59]. However, later, we proposed to refine the skin probability relying on the textural features [9] and to use the refined probability for computing the local cost  $\gamma_p$ .

The textural features are incorporated into the DSPF space, later exploited to refine the skin probability. In order to obtain the DSPF space, the *basic image features* are first extracted from the skin probability map. They consist of the following features: (i) the *median* and (ii) *minimal* values, (iii) *standard deviation*, and (iv) the *difference between the maximum and minimum*, computed in three kernels:  $5 \times 5$ ,  $9 \times 9$ , and  $13 \times 13$  pixels. In addition, the raw skin probability value is appended to this feature vector, as it is the principal source of the discriminating information between skin and non-skin pixels. We considered exploiting more advanced textural descriptors, for example, local binary patterns [64]; however, it has not improved the results. The selected features are aimed at extracting the roughness of the skin probability map rather than finding a repeatable pattern, and this can effectively be done using these simple statistics. Overall, every pixel  $x$  is transformed into an  $M$ -dimensional basic feature vector  $u_x$ , where  $M = 13$ . Using linear

discriminant analysis, the dimensionality of the basic image feature space is reduced to  $m = 2$  dimensions in the DSPF space.

Subsequently, a pixel of maximum skin probability is found in the skin probability map eroded using a large ( $15 \times 15$ ) kernel; it should be larger than the kernels used for extracting basic image features. This pixel is termed the *reference pixel r*, and the distance between  $r$  and every pixel in the image is computed in the DSPF space:

$$\mathcal{D}(x) = \left[ \sum_{i=1}^m (v_i^{(x)} - v_i^{(r)})^2 \right]^{1/2}, \quad (8)$$

where  $v_i^{(x)}$  is the  $i$ th dimension of the DSPF vector obtained for the pixel  $x$ . This operation converts the input skin probability map into the DSPF skin map, which is normalized and used for computing the destination-probability cost  $\gamma_p$ .

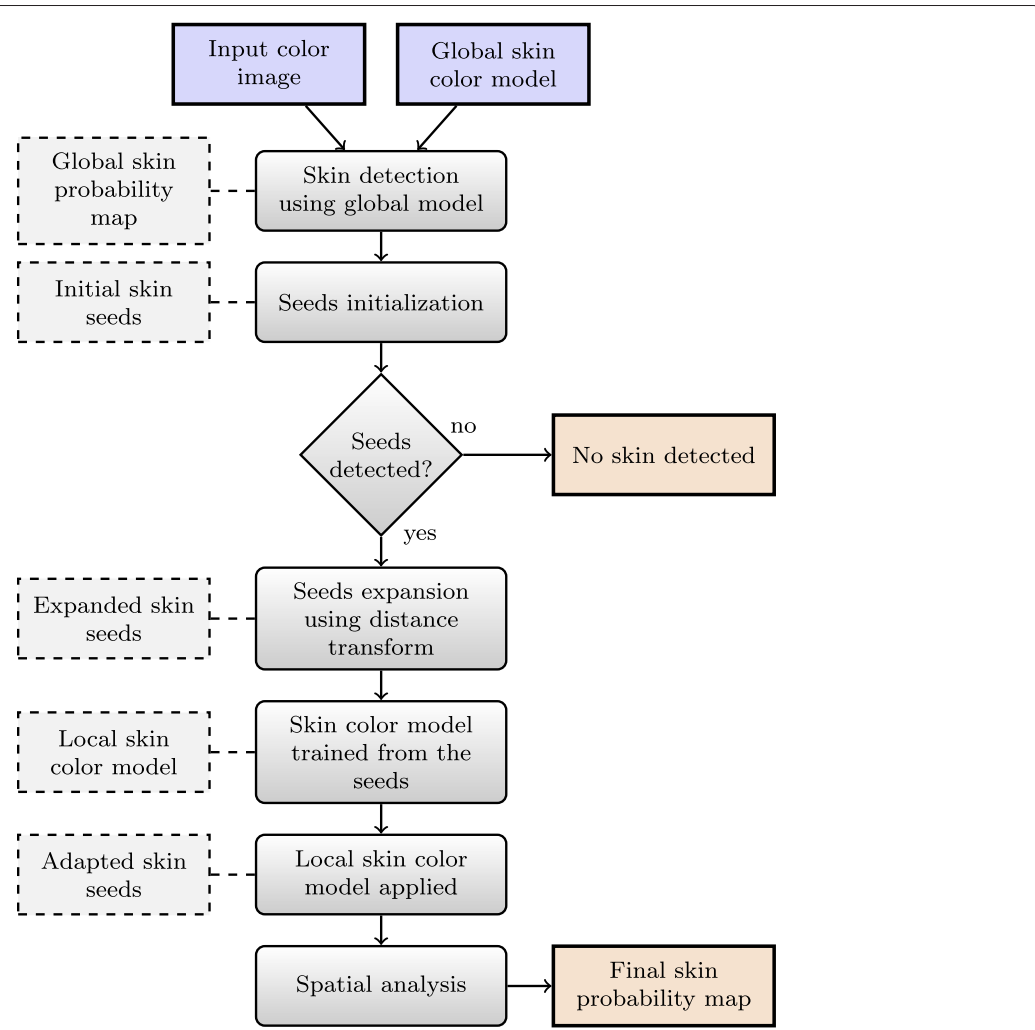


**Figure 1** Flowchart of the proposed skin segmentation process.

#### 4 Skin segmentation using self-adaptive seeds

In this section, we present the details of the proposed approach. Compared with our earlier methods, here, our main contribution lies in introducing a new technique for extracting adaptive seeds, which does not require any skin sample be given *a priori* for the adaptation. Instead of exploiting a face detector to acquire the skin sample, we analyze the skin probability map  $\mathcal{P}_S$  obtained from the input color image  $\mathcal{I}$  using a global skin color model. At first, our algorithm determines whether the image presents any skin pixels at all, and subsequently, it extracts the skin sample that is used to adapt the skin model and to build the seeds. Furthermore, we elaborate on the adaptation scheme we introduced in [11] and apply new metrics to compute local costs for DT [59]. These metrics (Equations 5 to 7) are used for creating the seeds, as well as they are utilized for the final ‘skinniness’ propagation.

#### 4.1 Algorithm outline

A flowchart of our method is presented in Figure 1, and examples of outcomes obtained at subsequent stages of the processing chain are demonstrated in Figure 2. First of all, an input image (Figure 2(a)) is converted into a skin probability map (Figure 2(b)) using a global skin color model based on the Bayesian classifier (the darker shade indicates higher skin probability). The obtained skin probability map is processed to determine the *initial skin seeds* (annotated as red pixels inside the black regions in Figure 2(c)). Here, our goal is to extract a sample of skin pixels with high precision, without including the non-skin pixels. Although it is crucial that the seeds are detected in every ground-truth skin blob, this is not critical at this stage, as the seeds are transferred to other regions later. An important problem here is to avoid finding the initial skin seeds in the images which do not contain human skin at all; otherwise, the algorithm may adapt the skin model

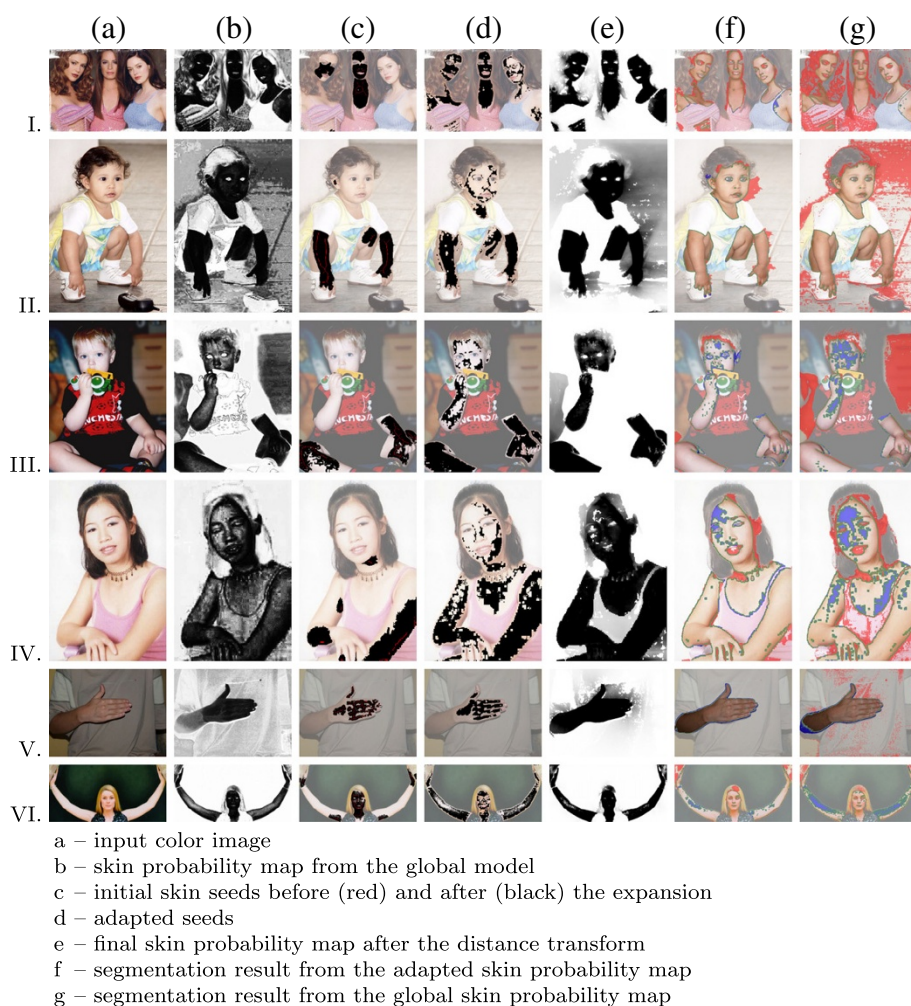


**Figure 2 Outcomes obtained at subsequent steps of the adaptive skin segmentation process.** The presented images (I to IV and VI) come from the publicly available ECU benchmark data set [65]. The image V comes from the HGR data set [9].

to some non-skin regions, increasing the false-positive rate. The exact procedure on how the initial seeds are determined is described later in Section 4.2.

Subsequently, the initial seeds are expanded using DT to include more skin pixels (black regions in Figure 2(c)). Again, the primary goal at this stage is to keep the false-positive rate at the smallest possible level; hence, the conditions for adjoining the pixels should be strict. From the expanded seeds, a local skin color model is trained and applied to the image in order to determine the final seeds for the

propagation (black regions in Figure 2(d)). Here, the aim is to find at least a single seed in every ground-truth skin region while keeping the false-positives low. It can be seen from Figure 2(d) (images I to IV) that the adapted seeds appear in the skin regions which were not covered by the initial skin seeds, while they are absent in the background. For image V, the seeds are not transferred to new skin regions, but the adaptation allows the seeds to be better distributed in the regions already covered by the expanded seeds. Also, an interesting case is image VI; here, the adaptation almost does not modify the

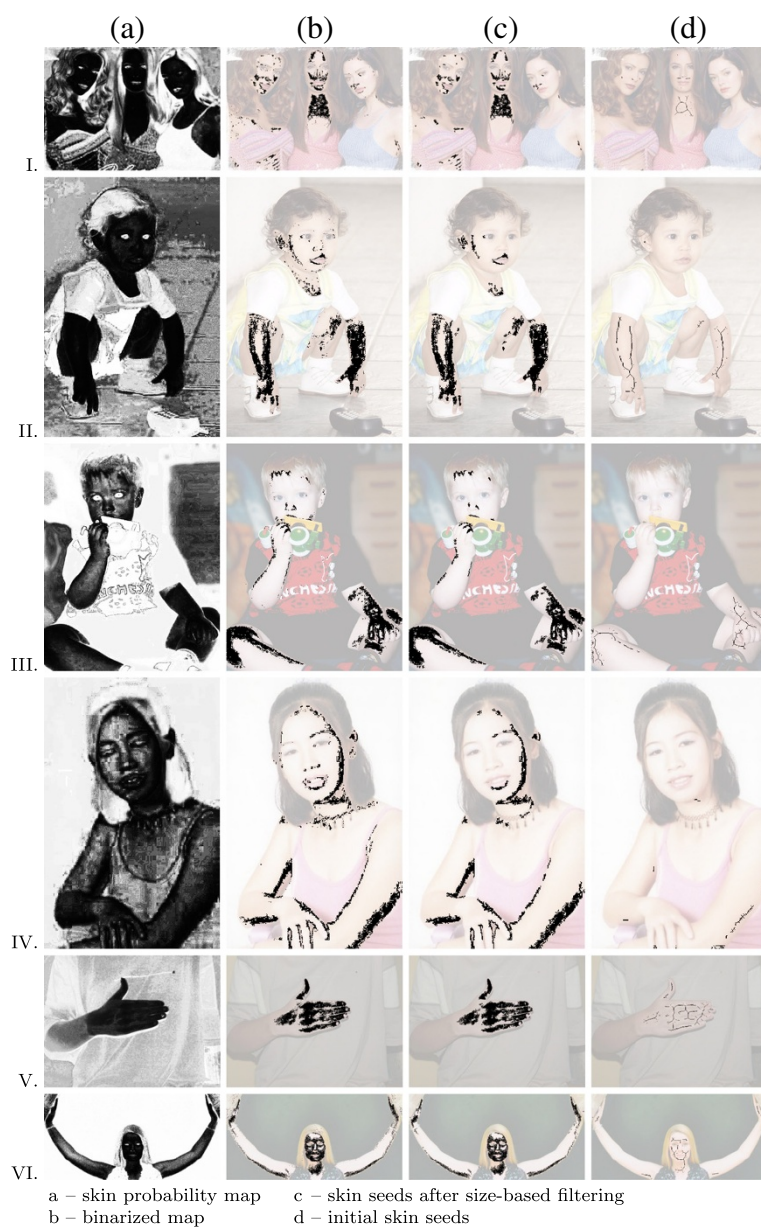


**Figure 3 Subsequent steps of extracting initial skin seeds from skin probability maps.** The presented images (I to IV and VI) come from the publicly available ECU benchmark data set [65]. The image V comes from the HGR data set [9].

position of the expanded seeds; however, eventually, the initial seeds occur sufficient to propagate the ‘skinniness’ over the entire skin area. The details of the seed transfer are given in Section 4.3.

From the final seeds, the ‘skinniness’ is propagated over the image to obtain the final skin probability map (Figure 2(e)), which is binarized to extract the skin regions (see Figure 2(f), where the red tone indicates false-positive pixels, the blue tone false-negatives, and the green one boundaries of the true-positive regions).

In Figure 2(g), we present the segmentation results obtained from the global skin probability maps (from Figure 2(b)). For several images (I to III), the adaptation substantially reduced the false-positives (which were caused by the background objects having skin-like color). Both the false-positives and false-negatives were reduced for the images III to V, and in the case of image VI, the false-negative rate was decreased.

#### 4.2 Extracting initial skin seeds

This stage consists in finding initial skin samples, from which the proper seeds for propagation are later created. In our method, this is achieved exclusively based on the analysis of a skin probability map obtained using a global skin color model (we utilize the Bayesian classifier here; however, other skin color models may also be exploited for this purpose). The initial skin seeds are extracted relying on the skin probability histogram and by analyzing the pixels in the spatial domain.

The algorithm for finding the initial seeds is outlined in Algorithm 1. First, we compute the integrated histogram  $\mathcal{H}$  (line 1) of the skin probability map  $\mathcal{P}_S$  to find the value of a dynamic threshold  $t_{seed}$ , which selects  $\mathcal{R}_{seed} = 5\%$  pixels, whose probability is above  $t_{seed}$  (line 2). Afterwards, we determine the reference

pixel  $r$  that indicates the maximum probability value in the eroded skin probability map  $\mathcal{P}_S^{\min}$  (line 5). Subsequently, we compute the *reference skin probability*  $P_r$  (line 6) as the minimum probability value in the dilated skin probability map  $\mathcal{P}_S^{\max}$  within the  $15 \times 15$  neighborhood of the reference pixel ( $\mathcal{N}_{15 \times 15}(r)$ ). Basically, if the reference pixel presents the skin indeed, then the value of the reference skin probability  $P_r$  should be high.

Based on the values of  $P_r$  and  $t_{seed}$ , we take the decision (Algorithm 1, line 8) whether an image contains skin pixels at all (hence, we detect skin at the image level). This is an important step of our algorithm, as false-positive detection would lead to adapting the skin color model to non-skin pixels, significantly decreasing the overall segmentation precision. On the other hand, false-negative detection would mean that the entire skin area in the incorrectly classified image is rejected. We apply fairly simple rules here that consist in checking whether the  $P_r$  and  $t_{seed}$  values are above the thresholds  $\mathcal{T}_r^P = 0.24$  and  $\mathcal{T}_{seed}^P = 0.12$ , respectively. Efficacy of this technique is discussed later in Section 5.

If the image-level skin detection is positive, then the seeds are extracted by binarizing the skin probability map using the  $t_{seed}$  threshold (Algorithm 1, line 9). We have observed that the false-positive pixels are scattered in the binarized image, while the true-positive pixels are organized in spatially consistent groups. Following this observation, we use only 10% of the largest blobs (line 11). These blobs are additionally subject to the erosion (line 13) to eliminate the blobs having small area. Finally, the seeds are subject to the morphological skeletonization (line 14), which further reduces the false-positives. The results obtained in subsequent steps of the initial skin seeds extraction are presented in Figure 3.

---

#### Algorithm 1 Initial skin seeds generation

**Require:**  $\mathcal{P}_S$

- 1:  $\mathcal{H} \leftarrow \text{FindIntegratedHistogram}(\mathcal{P}_S);$
- 2:  $t_{seed} \leftarrow \text{FindThreshold}(\mathcal{H}, \mathcal{R}_{seed});$
- 3:  $\mathcal{P}_S^{\min} \leftarrow \text{Erode}(\mathcal{P}_S, 15);$
- 4:  $\mathcal{P}_S^{\max} \leftarrow \text{Dilate}(\mathcal{P}_S, 15);$
- 5:  $r \leftarrow \text{FindMaximum}(\mathcal{P}_S^{\min});$
- 6:  $P_r \leftarrow \text{FindMinimum}(\mathcal{P}_S^{\max}, \mathcal{N}_{15 \times 15}(r));$
- 7:  $\mathcal{S}^0 \leftarrow \{0\};$
- 8: **if**  $t_{seed} \geq \mathcal{T}_{seed}^P$  **and**  $P_r \geq \mathcal{T}_r^P$  **then**
- 9:      $\mathcal{S}^0 \leftarrow \text{Binarize}(\mathcal{P}_S, t_{seed});$
- 10:     $\mathcal{B} \leftarrow \text{FindBlobs}(\mathcal{S}^0);$
- 11:     $\mathcal{B} \leftarrow \text{FilterBlobs}(\mathcal{B});$
- 12:     $\mathcal{S}^0 \leftarrow \text{Render}(\mathcal{B});$
- 13:     $\mathcal{S}^0 \leftarrow \text{Erode}(\mathcal{S}^0, 11);$
- 14:     $\mathcal{S}^0 \leftarrow \text{MorphologicalSkeleton}(\mathcal{S}^0);$
- 15: **end if**

- ▷ Skin probability map obtained using a global model
- ▷  $\mathcal{R}_{seed}$  (%) pixels in  $\mathcal{P}_S$  have skin probability over  $t_{seed}$ 
  - ▷ Erosion using a  $15 \times 15$  kernel
  - ▷ Dilation using a  $15 \times 15$  kernel
  - ▷ Reference pixel  $r$  found in the eroded  $\mathcal{P}_S$
- ▷ Reference skin probability  $P_r$  found in the dilated  $\mathcal{P}_S$ 
  - ▷ Mask of the initial seeds (zeroed at this step)
  - ▷ Skin detection at the image level
- ▷  $\mathcal{P}_S$  is binarized with a threshold  $t_{seed}$  to get the seeds
  - ▷ The seeds  $\mathcal{S}^0$  are represented as a set of blobs  $\mathcal{B}$ 
    - ▷ 10% of the largest blobs are selected
    - ▷  $\mathcal{S}^0$  gets a mask of the filtered blobs
      - ▷ Isolated small blobs are removed
    - ▷  $\mathcal{S}^0$  presents a mask of the initial seeds

#### 4.3 Seed expansion and adaptation

The initial skin seeds are characterized with two general properties (confirmed experimentally): (i) the seeds indicate skin regions with very high precision (i.e., they contain very few false-positives), and (ii) they are not present in every ground-truth skin blob (see Figure 2(c)). The first property makes the seeds appropriate to initiate DT in order to determine the boundaries of those skin regions, in which the seeds appear. However, the second property means that the ‘skinness’ cannot be propagated in the spatial domain to non-covered skin blobs; hence, the color space must be used for transferring the ‘skinness’. This transfer is achieved by creating a local skin color model from the initial skin seeds and applying it to the entire image. After this operation, the seeds are expected to appear in every skin blob, and they are used for the final propagation.

Overall, the skin segmentation algorithm, including the detailed procedure for extracting the final seeds, is given in Algorithm 2. After obtaining the initial seeds, they are expanded using DT (line 3) to include more skin pixels (this forms the *expanded skin seeds*  $\mathcal{S}^E$ ). Without the expansion, the model built from the initial seeds would not be sufficiently representative and the seeds would not be correctly transferred in the color space. However, the expansion must be done carefully to avoid including non-skin pixels, which could eventually lead to transferring the seeds also into the background. We investigated various local costs for obtaining  $\mathcal{S}^E$  (termed  $\gamma_\Delta^E$ ); however, in all the cases, we impose the cost boundary  $\mathcal{T}_\Gamma = 3 \cdot \overline{\gamma_\Delta^E}$ , where  $\overline{\gamma_\Delta^E}$  is the average local cost computed within the image. Furthermore, we do not use the costless propagation here (i.e.,  $\mathcal{T}_0^P = 0$ ). This limits DT to the very neighborhood of the initial seeds, and the expanded seeds  $\mathcal{S}^E$  are formed of the pixels, whose total path cost  $\Gamma$  is a finite number (see Figure 2(c)).

---

#### Algorithm 2 Proposed self-adaptive skin segmentation

**Require:**  $\mathcal{I}, P_g(\mathcal{C}_s|\nu)$

- 1:  $\mathcal{P}_S^{(global)} \leftarrow \text{DetectSkin}(\mathcal{I}, P_g(\mathcal{C}_s|\nu));$
- 2:  $\mathcal{S}^0 \leftarrow \text{FindInitialSeeds}(\mathcal{P}_S^{(global)});$
- 3:  $\mathcal{S}^E \leftarrow \text{SeedsDistanceTransform}(\mathcal{S}^0, \mathcal{I}, \mathcal{P}_S^{(global)});$
- 4:  $P_l(\mathcal{C}_s|\nu) \leftarrow \text{LearnSkinModel}(\mathcal{I}, \mathcal{S}^E);$
- 5:  $\mathcal{P}_S^{(local)} \leftarrow \text{DetectSkin}(\mathcal{I}, P_l(\mathcal{C}_s|\nu))$
- 6:  $\mathcal{S}^A \leftarrow \text{Binarize}(\mathcal{P}_S^{(local)}, \mathcal{T}_A^P);$
- 7:  $\mathcal{S}^A \leftarrow \text{Erode}(\mathcal{S}^A, 5);$
- 8:  $\mathcal{P}_S \leftarrow \text{FinalDistanceTransform}(\mathcal{S}^A, \mathcal{I}, \mathcal{P}_S^{(local)});$

After expanding the initial seeds, they are transferred to other image regions in the color space domain. This is performed as follows. First, a local skin color model is learned from the pixels that lie within the expanded seeds (Algorithm 2, line 4). Subsequently, this model is used to detect skin in the entire image (line 5), and the local skin probability map  $P_l(\mathcal{C}_s|\nu)$  is obtained. We have investigated two techniques for creating the local model, namely (i) from the color histogram and (ii) using a single multivariate Gaussian. The histogram-based approach takes into account only the skin color distribution, from which the skin probability  $P(\nu|\mathcal{C}_s)$  is directly obtained. As suggested in many works [2,17], we decrease the number of histogram bins per channel to achieve higher generalization. Following the second technique, the skin probability for a color  $\nu$  is obtained as

$$P(\nu) = \frac{1}{\sqrt{(2\pi)^3 |\Sigma|}} \exp \left[ -0.5(\nu - \bar{\nu})^T \Sigma^{-1} (\nu - \bar{\nu}) \right], \quad (9)$$

where  $\Sigma$  is a  $3 \times 3$  covariance matrix and  $\bar{\nu}$  is the mean color in the RGB color space, obtained for the skin pixels within the expanded seeds.

Finally, the local skin probability map  $P_l(\mathcal{C}_s|\nu)$  is binarized using the threshold  $\mathcal{T}_A^P$  to obtain the *adapted skin seeds*  $\mathcal{S}^A$  (Algorithm 2, line 6), which completes the seed transfer stage. The local model is trained using the skin pixels from the expanded seeds, characterized by low rate of false-positive pixels. This implies very high skin detection precision, and there are few false-positives among the pixels with non-zero skin probability in  $P_l(\mathcal{C}_s|\nu)$ . Therefore, we apply a fairly low binarization threshold of  $\mathcal{T}_A^P = 0.02$  (we have found that the algorithm is little sensitive to this value within the range  $0 < \mathcal{T}_A^P < 0.1$ ). After binarization, the seeds are eroded with a small  $5 \times 5$  kernel (line 7), which eliminates isolated positive pixels and shrinks the larger seeds. The shrinking is beneficial as the adapted seeds may be located at the boundaries of the

- ▷ Input color image and global skin color model
- ▷ Skin detection using global skin color model
- ▷ Initial skin seeds determined using Algorithm 1
- ▷ The initial seeds are expanded
- ▷ Local skin color model is build within  $\mathcal{S}^E$
- ▷ Skin detection using local skin color model
- ▷ Adapted skin seeds
- ▷  $\mathcal{S}^A$  are slightly shrunk
- ▷ The final skin probability map is obtained

skin regions. If the propagation is initiated from them, then some background pixels could be misclassified. Naturally, the shrinking eliminates some true-positive skin pixels, but then they are correctly rejoined back during the propagation.

Finally, the ‘skinniness’ is propagated from the adapted seeds in the image using the local difference costs  $\gamma_{\Delta}^F$  (Algorithm 2, line 8), and the final skin probability is obtained from the normalized map of distances as outlined earlier in Section 3.2. Depending on how the destination-probability cost  $\gamma_p$  is computed for expanding the seeds and for propagating the ‘skinniness’, we consider two variants of our method. This cost may be computed using the raw skin probability obtained from the global model (termed raw probability (RP)-based propagation) or alternatively, the DSPF skin map may be used for this purpose as outlined in Section 3.3 (termed DSPF-based propagation).

## 5 Experimental validation

We have validated the proposed algorithm using two data sets, namely (i) the ECU benchmark database [65] and (ii) our hand gesture recognition (HGR) set of hand images (available at <http://sun.aei.polsl.pl/~mkawulok/gestures>). Both data sets encompass ground-truth skin-presence binary masks. Four thousand images from the ECU set were acquired in uncontrolled lighting conditions, and skin-color objects often appear in the background, which makes the skin segmentation more difficult. The HGR data set contains 1,293 images of gestures presented by 30 individuals. The data were acquired in both controlled and uncontrolled conditions.

All the algorithms were implemented in C++. The experiments were conducted using a computer equipped with an Intel Core i7-3740QM 2.7 GHz (16 GB RAM) processor.

Two thousand images from the ECU set were used to train the Bayesian classifier and to determine the DSPF space. The remaining 2,000 images from the ECU set and all of the images from the HGR set were used as the test set. The test set consists of the images, in which the faces were detected with the method described in [66], so that our method can be compared with face-based adaptation schemes. The lists of images used for training and testing are available in Additional file 1.

We have compared our technique with several state-of-the-art methods, namely with (i) several global pixel-wise skin detectors [14–16], (ii) with methods that utilize spatial analysis and textural features [9,59,61], and (iii) with face-based adaptation schemes [11,40].

### 5.1 Evaluation metrics

The obtained results were compared with the ground-truth data to determine the number of correctly classified

pixels (i.e., TP and *true-negatives* (TN)) as well as the number of misclassified pixels (i.e., FN and FP). From these values, we use the following ratios to indicate the detection accuracy:

1. *Recall*:  $rec = TP/(FN + TP)$ , i.e., the percentage of the ground-truth skin pixels correctly classified as skin.
2. *Precision*:  $prec = TP/(TP + FP)$ , i.e., the percentage of correctly classified pixels out of all the pixels classified as skin.
3. *F-measure*: the harmonic mean of precision and recall. Here, the acceptance threshold was set to a value, for which the *F*-measure was maximal (precision and recall values are also quoted using the same threshold). Naturally, the same value of the threshold is applied to all of the images in the test set within a single experiment.
4. *False-positive rate*:  $\delta_{fp} = FP/(FP + TN)$ , i.e., the percentage of background pixels misclassified as skin.
5. *Minimal error*:  $\delta_{min} = 0.5 \cdot (\delta_{fp} + (1 - rec))$ . Here, the acceptance threshold was set to a value, for which  $\delta_{min}$  is minimal for the test set.

It is worth noting that the *F*-measure and the minimal error  $\delta_{min}$  are usually obtained using different acceptance thresholds, and they represent different properties of the detector. The minimal error is determined at a higher recall obtained at a cost of larger false-positive rate. Hence, these two values are quoted in the paper in order to provide better evaluation.

The precision, recall, and false-positive rate depend on the acceptance threshold. Their mutual dependence can be rendered in a form of precision-recall and receiver operating characteristic (ROC) curves [67,68], which are also presented to evaluate the investigated skin detectors.

In order to assess the performance for the images that do not contain human skin at all, we excluded the skin regions from the images in the ECU and HGR sets. These data sets include the ground-truth skin presence masks, and based on them, it was possible to exclude the skin regions from processing. We subjected these images to skin detection and measured the false-positive rate (termed  $\delta_{fp}^{ns}$ ).

In the case of the seed detection, the recall is usually very low, while the precision is expected to be high. However, as it was explained earlier, it is crucial that the seeds appear in every ground-truth skin region. Otherwise, a region without a seed will not be rejoined to the skin class during the propagation (unless the ‘skinniness’ is propagated through the background, which in general should be avoided). In order to measure whether the seeds are correctly located, we measure the *potential recall* ( $rec_{seed}$ ); we assume that if at least a single seed is positioned inside

**Table 2**  $F$ -measure and  $\delta_{\min}$  obtained using the DSPF-based propagation with different thresholds ( $\mathcal{T}_{seed}^P$  and  $\mathcal{T}_r^P$ )

$\mathcal{T}_{seed}^P$	$\mathcal{T}_r^P$	ECU data set		HGR data set	
		$F$ -measure ( $\delta_{\min}$ )	$\delta_{fp}^{ns}$	$F$ -measure ( $\delta_{\min}$ )	$\delta_{fp}^{ns}$
0.00	0.00	0.8415 (7.19%)	12.81%	0.9564 (2.49%)	76.73%
0.00	0.12	0.8415 (7.19%)	12.80%	0.9564 (2.49%)	33.32%
0.00	0.24	0.8411 (7.22%)	12.79%	0.9564 (2.49%)	20.97%
0.00	0.36	0.8408 (7.24%)	12.72%	0.9550 (2.63%)	8.85%
0.12	0.00	0.8415 (7.19%)	12.68%	0.9562 (2.52%)	13.35%
0.12	0.12	0.8415 (7.19%)	12.68%	0.9562 (2.52%)	13.35%
0.12	0.24	0.8411 (7.22%)	12.67%	0.9562 (2.52%)	10.51%
0.12	0.36	0.8408 (7.24%)	12.61%	0.9547 (2.67%)	5.79%
0.24	0.00	0.8405 (7.26%)	12.47%	0.9452 (3.66%)	7.03%
0.24	0.12	0.8405 (7.26%)	12.47%	0.9452 (3.66%)	7.03%
0.24	0.24	0.8405 (7.26%)	12.47%	0.9452 (3.66%)	6.88%
0.24	0.36	0.8405 (7.26%)	12.42%	0.9452 (3.66%)	4.90%
0.36	0.00	0.8402 (7.28%)	11.94%	0.9280 (5.22%)	3.16%
0.36	0.12	0.8402 (7.28%)	11.94%	0.9280 (5.22%)	3.16%
0.36	0.24	0.8402 (7.28%)	11.94%	0.9280 (5.22%)	3.16%
0.36	0.36	0.8402 (7.28%)	11.92%	0.9280 (5.22%)	3.10%

Italicized values indicate the selected configuration.

a certain ground-truth skin region, then the whole region is correctly classified as skin. For the seeds, we do not quote the false-positive rate, as it is usually close to zero due to the small number of seed pixels compared to the number of all the pixels in an image. The precision is much a better measure here.

## 5.2 Parameter tuning and sensitivity analysis

In this section, we report how we selected the parameters and models used in our method, and we analyze their influence on the obtained scores.

First of all, we focused on the image-level skin detection (as shown in Algorithm 1, line 8), which is controlled with two thresholds:  $\mathcal{T}_{seed}^P$  and  $\mathcal{T}_r^P$ . In Table 2, we demonstrate the  $F$ -measure and the minimal error  $\delta_{\min}$  (given in the brackets) for images that contain skin, and we show the false-positive rate  $\delta_{fp}^{ns}$  for the images without skin. It can be seen that in general  $\delta_{fp}^{ns}$  decreases if the thresholds are high (and more restrictive), but obviously this affects the detection scores for the images that contain human skin. It is worth noting that  $\delta_{fp}^{ns}$  for the ECU set is much less sensitive to the thresholds than for the HGR set. If it is assumed

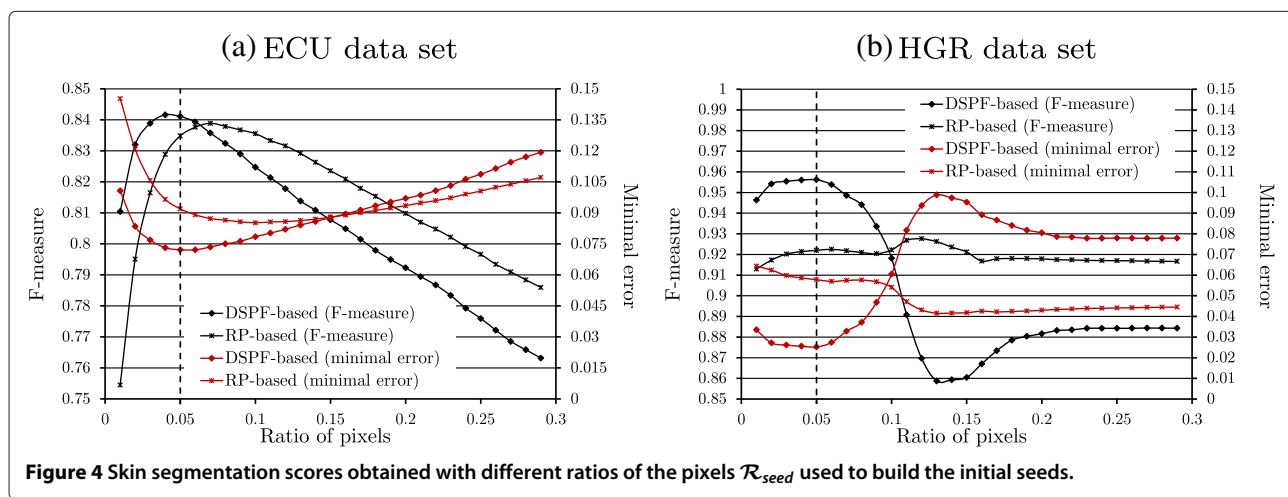


**Figure 4** Skin segmentation scores obtained with different ratios of the pixels  $R_{seed}$  used to build the initial seeds.

**Table 3 F-measure and minimal error  $\delta_{\min}$  (given in brackets) obtained using different local propagation costs**

$\gamma_p \downarrow$	$\gamma_{\Delta}^E \downarrow \gamma_{\Delta}^F \rightarrow$	ECU data set			HGR data set		
		$\gamma_{\Delta}^{(HL)}$	$\gamma_{\Delta}^{(RGB)}$	$\gamma_{\Delta}^{(SP)}$	$\gamma_{\Delta}^{(HL)}$	$\gamma_{\Delta}^{(RGB)}$	$\gamma_{\Delta}^{(SP)}$
Gaussian							
RP	$\gamma_{\Delta}^{(HL)}$	0.8511 (8.20%)	0.8547 (7.71%)	0.8460 (8.05%)	0.9132 (6.75%)	0.9130 (6.75%)	0.9157 (6.55%)
	$\gamma_{\Delta}^{(RGB)}$	0.8469 (8.58%)	0.8511 (8.00%)	0.8440 (8.28%)	0.9136 (6.73%)	0.9134 (6.73%)	0.9159 (6.55%)
	$\gamma_{\Delta}^{(SP)}$	0.8499 (8.43%)	0.8535 (7.96%)	0.8419 (8.44%)	0.9136 (6.73%)	0.9135 (6.74%)	0.9155 (6.57%)
DSPF	$\gamma_{\Delta}^{(HL)}$	0.8411 (7.22%)	0.8409 (7.10%)	0.8339 (7.77%)	0.9562 (2.52%)	0.9538 (2.79%)	0.9545 (2.55%)
	$\gamma_{\Delta}^{(RGB)}$	0.8425 (7.32%)	0.8420 (7.26%)	0.8355 (7.79%)	0.9564 (2.50%)	0.9540 (2.78%)	0.9548 (2.56%)
	$\gamma_{\Delta}^{(SP)}$	0.8388 (7.34%)	0.8387 (7.22%)	0.8360 (8.04%)	0.9566 (2.49%)	0.9541 (2.76%)	0.9301 (5.70%)
Histogram							
RP	$\gamma_{\Delta}^{(HL)}$	0.8330 (9.55%)	0.8389 (8.83%)	0.8341 (9.08%)	0.9204 (5.99%)	0.9204 (5.98%)	0.9220 (5.84%)
	$\gamma_{\Delta}^{(RGB)}$	0.8286 (9.71%)	0.8320 (9.14%)	0.8283 (9.39%)	0.9221 (5.84%)	0.9220 (5.84%)	0.9226 (5.78%)
	$\gamma_{\Delta}^{(SP)}$	0.8313 (9.69%)	0.8348 (9.20%)	0.8266 (9.60%)	0.9221 (5.78%)	0.9220 (5.78%)	0.9215 (5.82%)
DSPF	$\gamma_{\Delta}^{(HL)}$	0.8353 (7.84%)	0.8347 (7.81%)	0.8295 (8.28%)	0.9555 (2.50%)	0.9539 (2.74%)	0.9520 (2.97%)
	$\gamma_{\Delta}^{(RGB)}$	0.8363 (8.01%)	0.8355 (8.01%)	0.8305 (8.35%)	0.9550 (2.56%)	0.9537 (2.79%)	0.9517 (3.04%)
	$\gamma_{\Delta}^{(SP)}$	0.8350 (7.85%)	0.8342 (7.82%)	0.8322 (8.70%)	0.9544 (2.57%)	0.9530 (2.78%)	0.9372 (4.70%)

The arrows indicate the column or row. Italicized values indicate the configuration used in the remaining experiments.

that every image contains the skin (i.e., both thresholds are set to zero), then  $\delta_{fp}^{ns}$  for the HGR set is extremely high, while for ECU it is at a moderate level. This is because the images in the ECU set contain uncontrolled multi-colored background, while the background in many images from the HGR set is uniform. In such cases, after adaptation, the entire background is classified as skin, while for ECU only some objects in the background are misclassified. Overall, we use  $\mathcal{T}_{seed}^P = 0.12$  and  $\mathcal{T}_r^P = 0.24$  (italicized in Table 2), which does not decrease the scores for skin images significantly, while  $\delta_{fp}^{ns}$  is at an acceptable level.

The scores obtained depending on the  $\mathcal{R}_{seed}$  ratio are presented in Figure 4. It can be seen from the plots that the algorithm is quite sensitive to this parameter; however,

in case of both data sets, the optimal value is around  $\mathcal{R}_{seed} = 0.05$  (marked with a vertical dashed line), and this value has been used in our experiments. In the case of the HGR set, the scores for the DSPF-based propagation deteriorate when  $\mathcal{R}_{seed}$  surpasses 0.05, but then (at about 0.15) they start improving again. In order to investigate this, we measured the precision and potential recall in the seeds (the plots are presented in Additional file 2). We have found that for the HGR set, the potential recall in the initial and expanded seeds temporarily decreases (for  $\mathcal{R}_{seed} \in [0.1; 0.15]$ ), because the true-positive blobs are eliminated due to the size-based filtering. However, for smaller values of  $\mathcal{R}_{seed}$ , the size-based filtering helps achieve higher precision in the initial seeds.

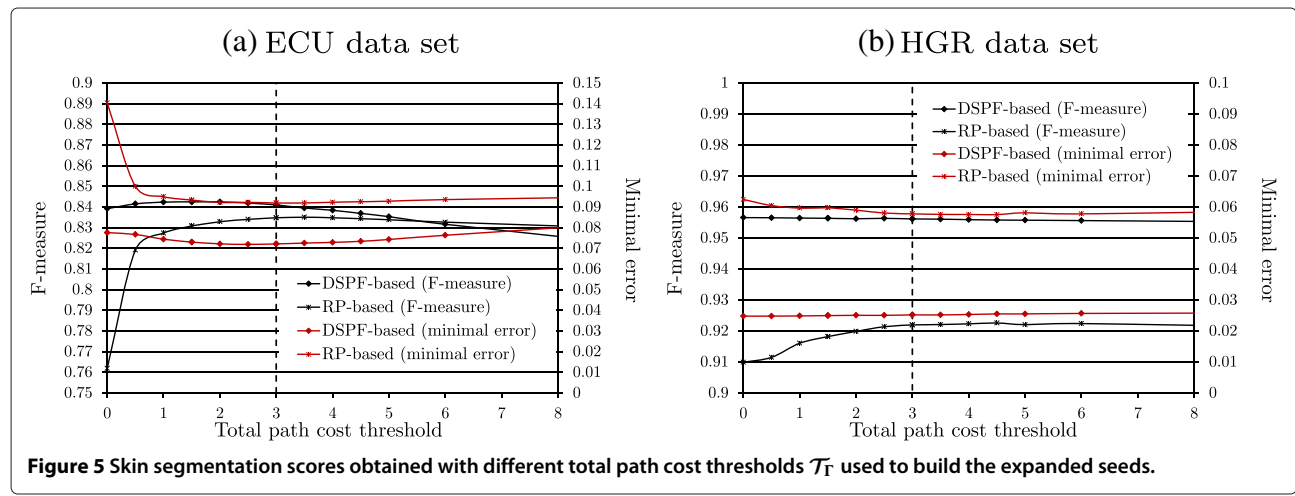


**Figure 5 Skin segmentation scores obtained with different total path cost thresholds  $\mathcal{T}_T$  used to build the expanded seeds.**

**Table 4 F-measure and minimal error  $\delta_{\min}$  (given in brackets) obtained using different local skin color models**

$\gamma_p \rightarrow$ ↓ Local skin color model	RP-based		DSPF-based	
	ECU data set	HGR data set	ECU data set	HGR data set
Gaussian	0.8535 (7.96%)	0.9135 (6.74%)	0.8411 (7.22%)	0.9562 (2.52%)
Histogram, 256 bins	0.8308 (9.42%)	0.9215 (5.80%)	0.8347 (8.00%)	0.9556 (2.51%)
Histogram, 128 bins	0.8348 (9.20%)	0.9220 (5.78%)	0.8353 (7.84%)	0.9555 (2.50%)
Histogram, 64 bins	0.8400 (8.82%)	0.9217 (5.86%)	0.8348 (7.56%)	0.9563 (2.43%)
Histogram, 32 bins	0.8328 (9.01%)	0.9145 (6.59%)	0.8257 (7.90%)	0.9559 (2.49%)
Histogram, 16 bins	0.8107 (9.95%)	0.9134 (6.67%)	0.8125 (8.62%)	0.9533 (2.69%)
Histogram, 8 bins	0.7906 (10.96%)	0.9138 (6.67%)	0.7982 (9.62%)	0.9481 (3.06%)

The arrows indicate the column or row. Italicized values indicate the selected configuration.

In Table 3, we present the scores obtained using different local costs utilized to build the expanded seeds ( $\gamma_{\Delta}^E$ ) and to propagate the final ‘skinness’ ( $\gamma_{\Delta}^F$ ). The local skin color model was trained using either a single multivariate Gaussian, or using the color histogram with 128 bins per channel. It may be seen from the table that the RP-based propagation is more sensitive to the costs used, and different settings are optimal for the ECU and HGR sets. In some cases, the *F*-measure for the ECU set is higher using RP, but overall it is the DSPF-based propagation which delivers high scores for both the ECU and HGR

sets. The italicized values indicate the configuration used in the remaining experiments.

The seeds are expanded depending on the total path cost boundary  $T_{\Gamma}$ , and the sensitiveness to this parameter is demonstrated in Figure 5. It may be observed that the scores are little dependent on this value, and we used  $T_{\Gamma} = 3$  in our experiments (marked with a vertical dashed line in the plots).

We have trained the local skin color model using a single multivariate Gaussian as well as using the color histogram with different numbers of bins per channel.

**Table 5 Skin detection scores computed in the seeds at subsequent processing steps**

	ECU data set			HGR data set		
	<i>F</i> -measure	<i>prec</i>	<i>rec<sub>seed</sub></i>	<i>F</i> -measure	<i>prec</i>	<i>rec<sub>seed</sub></i>
Initial seeds	0.9233	90.64%	94.08%	0.9943	99.22%	99.65%
Seeds expanded using the RP domain and $\gamma_{\Delta}^{(SP)}$ local costs to expand the seeds						
Expanded seeds	0.9279	90.10%	95.64%	0.9961	99.49%	99.73%
Adapted seeds (Gaussian)	0.9536	91.63%	99.41%	0.9967	99.72%	99.63%
Adapted seeds (H-256)	0.9511	92.32%	98.08%	0.9828	99.85%	96.76%
Adapted seeds (H-128)	0.9527	92.24%	98.50%	0.9845	99.83%	97.11%
Adapted seeds (H-64)	0.9518	91.49%	99.18%	0.9881	99.64%	98.00%
Adapted seeds (H-32)	0.9419	89.35%	99.58%	0.9954	99.35%	99.73%
Adapted seeds (H-16)	0.9153	84.56%	99.76%	0.9936	98.83%	99.90%
Adapted seeds (H-8)	0.8834	79.18%	99.88%	0.9918	98.38%	99.98%
Seeds expanded using the DSPF domain and $\gamma_{\Delta}^{(HL)}$ local costs to expand the seeds						
Expanded seeds	0.9337	91.41%	95.41%	0.9957	99.42%	99.73%
Adapted seeds (Gaussian)	0.9539	91.78%	99.29%	0.9958	99.43%	99.73%
Adapted seeds (H-256)	0.9515	92.91%	97.52%	0.9882	99.79%	97.87%
Adapted seeds (H-128)	0.9533	92.81%	98.00%	0.9888	99.74%	98.04%
Adapted seeds (H-64)	0.9546	92.06%	99.12%	0.9923	99.54%	98.92%
Adapted seeds (H-32)	0.9455	89.97%	99.62%	0.9959	99.29%	99.89%
Adapted seeds (H-16)	0.9246	86.13%	99.80%	0.9944	98.92%	99.97%
Adapted seeds (H-8)	0.8960	81.26%	99.85%	0.9919	98.42%	99.98%

H-*n* is the color histogram with *n* bins per channel.

**Table 6 Skin detection scores obtained using different methods for the ECU data set**

Method	Acceptance threshold set to maximize F-measure				Acceptance threshold set to minimize $\delta_{\min}$			
	F-measure	prec	rec	$\delta_{fp}^{ns}$	$\delta_{\min}$	rec	$\delta_{fp}$	$\delta_{fp}^{ns}$
Global Bayesian classifier [16]	0.7772	73.15%	82.89%	9.13%	12.13%	89.27%	13.52%	13.52%
Global model in ESS [14]	0.7434	68.07%	81.88%	11.79%	14.13%	87.76%	16.03%	16.03%
Chen's global model [15]	0.6896	55.30%	91.61%	23.11%	15.75%	91.61%	23.11%	23.11%
Wavelet-based hybrid detector [61]	0.7894	76.34%	81.73%	9.01%	12.28%	88.74%	13.31%	13.78%
Face-based adaptation in ESS [40]	0.7672	69.67%	85.35%	-	13.95%	89.85%	17.74%	-
Spatial analysis using RP [59]	0.8177	75.79%	88.78%	8.45%	9.87%	92.32%	12.06%	10.32%
Spatial analysis using DSPFs [9]	0.8303	78.09%	88.65%	9.06%	7.68%	93.28%	8.64%	12.08%
Face-based adaptive seeds [11]	0.8661	82.70%	90.92%	-	7.17%	94.06%	8.39%	-
Proposed method (RP-based)	0.8348	81.07%	86.04%	8.40%	9.20%	90.85%	9.25%	10.44%
Proposed method (DSPF-based)	0.8411	79.10%	89.79%	12.67%	7.22%	94.14%	8.57%	16.57%

Italicized values indicate the best score.

The obtained scores are presented in Table 4 (the italicized values indicate the selected configuration). For the ECU set, both RP-based and DSPF-based propagations deliver the best scores when the local model is learned with a Gaussian; however, in the case of RP, the scores for the HGR set are much worse than when using the histogram-based model. Also, analysis of the plots in Additional file 2 allows us to conclude that the Gaussian offers higher generalization than the histogram-based model.

Finally, in Table 5, we present the scores computed in the seeds at subsequent steps of their extraction. Here, we show the results for RP- and DSPF-based propagation, using different local costs  $\gamma_{\Delta}^E$ . It may be seen that for the ECU set, the potential recall and the F-measure increase substantially between the initial and adapted seeds. In the case of the HGR set, the potential recall is high already in the initial seeds; as in many cases, there is a single skin blob in these images, and it is already covered by the initial seeds. Overall, it is clear that the scores improve during

the seed extraction process, which justifies its subsequent steps.

### 5.3 Quantitative comparison

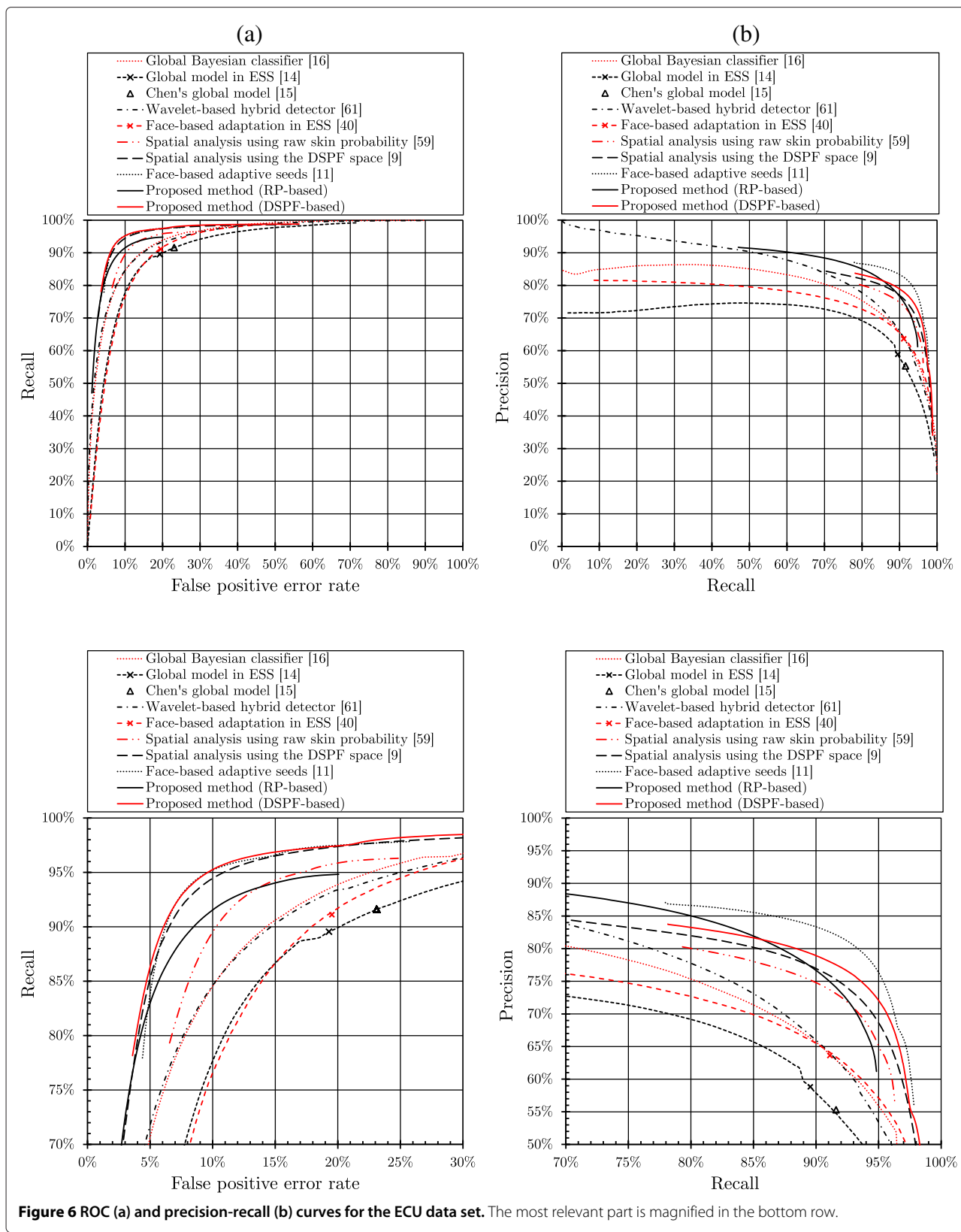
The scores obtained using a number of alternative state-of-the-art methods are presented in Tables 6 and 7. ROC and precision-recall curves are rendered in Figures 6 and 7. In the case of the ECU set, we have included two face-based adaptation methods [11,40]. Naturally, they were omitted for the HGR images as they do not present human faces. In the tables, we demonstrate the scores for two values of the acceptance threshold, for which the F-measure is maximal and the error  $\delta_{\min}$  is minimal, respectively.

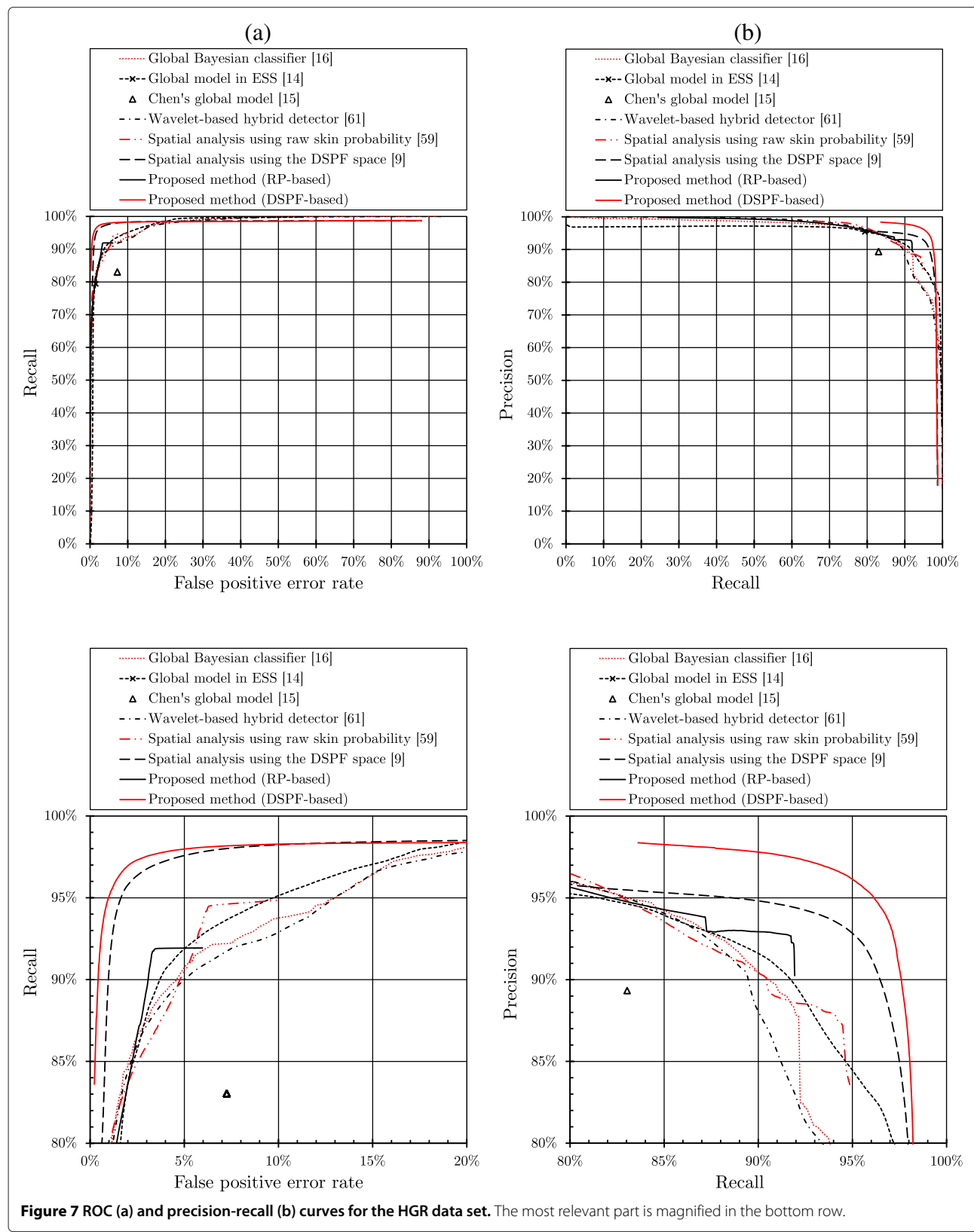
The methods operating in the ESS [14,40] offer binary skin classification, but we extended them so that they produce the continuous response. In the plots in Figures 6 and 7, each result for the original binary decision is indicated with a cross (obviously, it is positioned on the ROC or precision-recall curve).

**Table 7 Skin detection scores obtained using different methods for the HGR data set**

Method	Acceptance threshold set to maximize F-measure				Acceptance threshold set to minimize $\delta_{\min}$			
	F-measure	prec	rec	$\delta_{fp}^{ns}$	$\delta_{\min}$	rec	$\delta_{fp}$	$\delta_{fp}^{ns}$
Global Bayesian classifier [16]	0.9031	89.72%	90.92%	5.11%	7.05%	91.53%	5.63%	5.63%
Global model in ESS [14]	0.9090	90.76%	91.04%	4.31%	6.56%	91.81%	4.92%	4.92%
Chen's global model [15]	0.8607	89.33%	83.03%	7.26%	12.11%	83.03%	7.26%	7.26%
Wavelet-based hybrid detector [61]	0.8991	91.38%	88.49%	3.91%	7.50%	90.24%	5.25%	5.38%
Spatial analysis using RP [59]	0.9086	87.77%	94.17%	29.83%	5.91%	94.49%	6.30%	43.18%
Spatial analysis using DSPF [9]	0.9391	92.90%	94.94%	8.39%	3.06%	96.24%	2.37%	8.94%
Proposed method (RP-based)	0.9220	92.66%	91.74%	26.52%	5.78%	91.85%	3.41%	31.88%
Proposed method (DSPF-based)	0.9562	95.32%	95.92%	10.51%	2.52%	96.92%	1.96%	11.71%

Italicized values indicate the best score.





The method utilizing the face-based adaptive seeds [11] delivers the best scores for the ECU set, especially in terms of the precision-recall and the *F*-measure. The ROC curve and minimal error  $\delta_{\min}$  are virtually identical with those obtained with our DSPF-based approach. However, it must be noted that this method requires additional information delivered by a face detector. Here, we carefully selected those images, in which the faces are correctly detected, in order to demonstrate the maximal advantage that can be achieved using the face-based adaptation over the proposed self-adaptive method. The second face-based adaptation technique, which operates in ESS, improves the global skin color model in ESS, but it is not competitive compared with other techniques. For the HGR set, our adaptation scheme with DSPF-based propagation outperforms other methods, offering very high skin segmentation accuracy (*F*-measure is 0.9562 and  $\delta_{\min} = 2.52\%$ ).

We have also measured the false-positive rate ( $\delta_{fp}^{ns}$ ) for images that do not present human skin. As it was already mentioned, we used the same ECU and HGR images, in which the skin regions were excluded from processing, and we applied the same values of the acceptance threshold as in the case of the original images. In this way, we investigated whether and how the absence of skin regions influences the false-positive rate. This experiment was not executed for the face-based adaptation schemes, because after excluding the skin regions, the faces should not be detected at all. Obviously, for pixel-wise classification schemes, the false-positive rate is identical regardless of whether the skin is present in the image. For other methods, the false-positive rate is generally higher, as each of them adapts to some extent to the image. Overall, using the self-adaptive seeds with the DSPF-based propagation domain (the RP-based domain is more sensitive here),  $\delta_{fp}^{ns}$  is from 3.05% (ECU,  $\delta_{\min}$ ) to 6.08% (HGR,  $\delta_{\min}$ ) higher than obtained with the Bayesian classifier. This shows that the incorrect adaptation is a potential problem; however, we managed to limit its impact using a simple image-level skin detector. Also, this problem is common to all the adaptive methods, including the face-based schemes in case of false-positive face detection. Last, but not least, there are many applications, including hand pose estimation, where efficient skin segmentation is critical, and such errors can be mitigated at further processing stages (e.g., a hand shape would be unlikely to be matched, if the entire detected skin region is falsely-positive).

The average processing times required to process a  $512 \times 512$  image are quoted in Table 8. It may be observed that almost half of the computation time (i.e., 216.6 ms) is consumed to create the adaptive seeds. When a video stream is processed, the adaptation does not have to be performed for every frame as the scene usually does not change with a high frequency rate. This means that the

**Table 8 Average processing times for a  $512 \times 512$  image**

Method	Time (ms)
Global Bayesian classifier [16]	5.2
Global model in ESS [14]	4.8
Chen's global model [15]	0.8
Wavelet-based hybrid detector [61]	4,952.5
Face-based adaptation in ESS [40]	24.1
Spatial analysis using RP [59]	92.9
Spatial analysis using DSPF [9]	361.1
Face-based adaptive seeds [11]	130.5
Proposed method (RP-based)	232.9
Skin detection using global model	5.29
Skin seeds initialization	56.34
Expansion of the seeds	77.97
Adaptation of the seeds	19.49
Final spatial analysis	73.81
Proposed method (DSPF-based)	548.2
Skin detection using global model	5.34
Generation of the DSPF skin map	192.43
Skin seeds initialization	46.18
Expansion of the seeds	79.30
Adaptation of the seeds	91.17
Final spatial analysis	133.78

skin model can be adapted once for a given scene and then the stream can be processed at ca. three frames per second. Also, it may be seen that the RP-based propagation is much faster, because (i) the DSPF skin map does not have to be computed and (ii) the histogram-based adaptation is much faster than using a Gaussian model. Excluding the adaptation phase, the RP-based approach requires 79.1 ms, which allows processing over 12 frames per second. Overall, there are two time-consuming operations which could potentially be optimized, namely (i) generation of the DSPF skin map and (ii) the distance transform. The former includes a number of independent operations (the basic features are computed in several kernels), which may be executed in parallel to reduce the processing time. The main problem with the distance transform lies in non-linear access to the memory while processing the pixels popped from the priority queue used in the Dijkstra algorithm. Possibly, this may be improved by including the neighborhood criteria into the priority measure to avoid referring to the pixels far from each other in the memory, but this needs to be investigated.

#### 5.4 Qualitative comparison

In Figures 8 and 9, we present several examples of skin detection in ECU and HGR images, respectively. For images I to VIII in Figure 8, our method segments the



skin regions with high precision. Images IX and X are the examples of incorrect adaptation. Here, the background has a skin-like color, and the seeds are detected both in the skin, and in the background, resulting in very high false-positive errors. However, it is worth mentioning that the alternative detectors fail in these cases as well, except

for two face-based adaptation methods [11,40]. We also present several cases, in which the face-based adaptation is incorrect. In image VI, the face is rotated, and the facial region includes some background pixels, resulting in high false-positives. Also, images VII and VIII are quite interesting as the bearded VII and the soother VIII

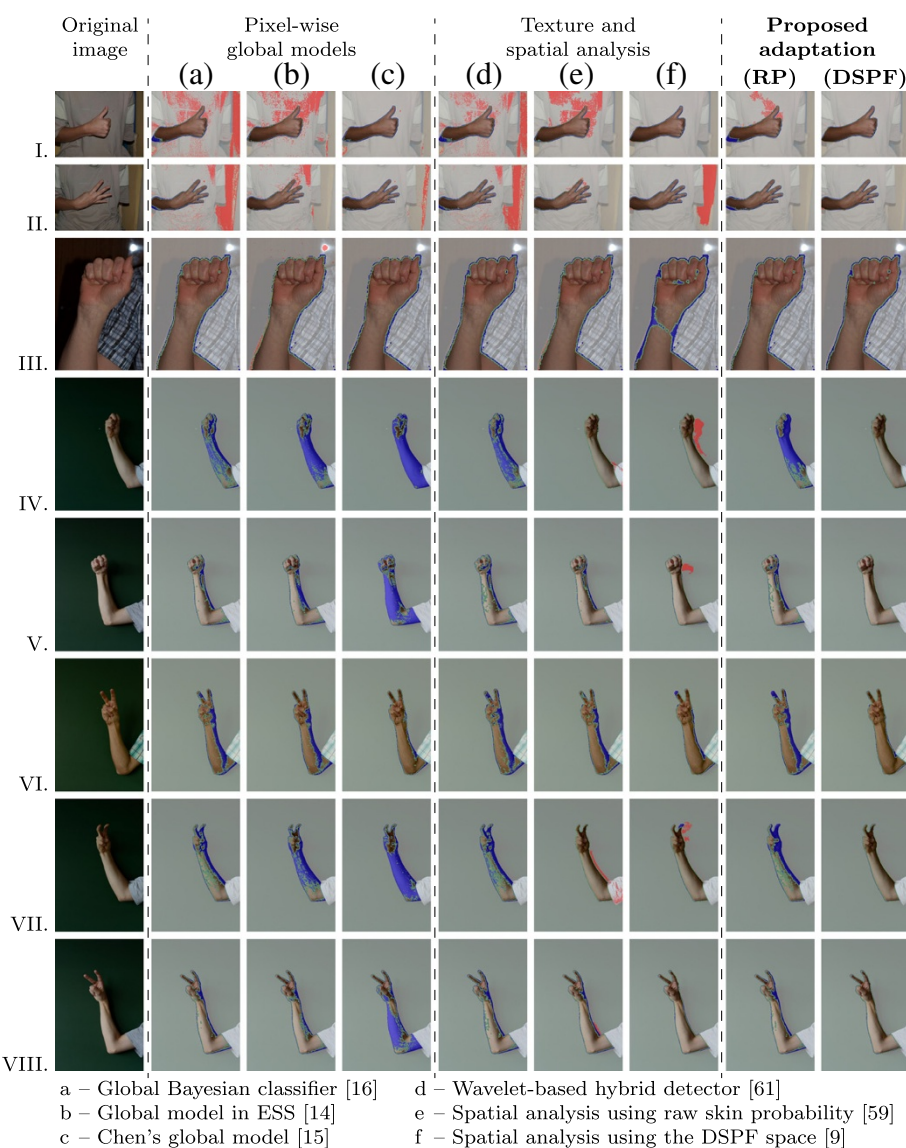


**Figure 9 Examples of skin segmentation for the HGR data set obtained using different methods.** The presented images come from the HGR data set [9].

appear inside the facial region, leading to incorrect adaptation. Naturally, this problem does not appear in our self-adaptive approach.

For the HGR images presented in Figure 9, our DSPF-based method offers almost perfect skin segmentation, and it clearly outperforms all the alternative algorithms. Also, comparing the results with [9], it is evident that using the adaptive seeds is more effective than the threshold-based seeds extraction.

## 6 Conclusions

In this paper, we proposed a new method for creating self-adaptive seeds for spatial-based skin segmentation. From the seeds, the 'skinniness' is propagated either using the raw

skin probability obtained from a global skin color model or using the probability computed in the DSPF space. Our extensive experimental study demonstrated that the DSPF domain is less sensitive to the method's parameters and outperforms all of the investigated methods both for the ECU and HGR data sets, except for our earlier face-based adaptation [11]. The raw probability domain is much more sensitive, which makes it difficult to tune; however, in some cases (for the ECU set), it delivered better results than the DSPF and also it is much less time consuming. Overall, we found it worth being reported as well.

Our main contribution consists in providing the adaptiveness without making the method dependent on any other information sources. This is the main advantage

over the face-based adaptation schemes, and we demonstrated that using the self-adaptive seeds, it is possible to obtain results comparable with the face-based adaptation. The benefits in case of images that do not present human faces are obvious, while there are also many examples presented in the paper, when the proposed adaptation method outperforms the face-based ones.

Our current research plans include combining the introduced adaptation technique with the face-based schemes, which may help in cases when the background pixels appear in the detected facial regions. Furthermore, we intend to improve the image-level skin detection; we have demonstrated in our experimental study that this is an important, while often disregarded, problem in adaptive skin color modeling. Last, but not least, the algorithm should be parallelized and optimized in order to make it suitable for processing video sequences.

## Additional files

**Additional file 1: Packed text files.** The files contain the names of the files used in the training and test set.

**Additional file 2: Supplementary figures.** The figures illustrate the detection accuracy in the skin seeds obtained with different ratios of the pixels  $\mathcal{R}_{seed}$  used to build the initial seeds.

## Competing interests

The authors declare that they have no competing interests.

## Acknowledgements

This work was supported by the Polish National Science Center (NCN) under the Grant: DEC-2012/07/B/ST6/01227. This work was performed using the infrastructure supported by POIG.02.03.01-24-099/13 grant: 'GeCONiI' Upper Silesian Center for Computational Science and Engineering. JK was supported by the European Union from the European Social Fund (grant agreement number: UDA-POKL.04.01.01-00-106/09).

Received: 16 July 2014 Accepted: 27 October 2014

Published: 29 November 2014

## References

1. P Kakumanu, S Makrogiannis, NG Bourbakis, A survey of skin-color modeling and detection methods. *Pattern Recognit.* **40**(3), 1106–1122 (2007)
2. M Kawulok, J Nalepa, J Kawulok, in *Lecture Notes in Computational Vision and Biomechanics: Advances in Low-Level Color Image Processing*, vol. 11, ed. by ME Celebi, B Smolka. Skin detection and segmentation in color images (Springer, Netherlands, 2014), pp. 329–366
3. S Bilal, R Akmeliaiwati, MJE Salami, AA Shafie, Dynamic approach for real-time skin detection. *J. Real-Time Image Process.* (2012). doi:10.1007/s11554-012-0305-2
4. J-S Lee, Y-M Kuo, P-C Chung, E-L Chen, Naked image detection based on adaptive and extensible skin color model. *Pattern Recognit.* **40**, 2261–2270 (2007)
5. H Kruppa, MA Bauer, B Schiele, in *Lecture Notes in Computer Science: Pattern Recognition*, vol. 2449, ed. by L Van Gool. Skin patch detection in real-world images (Springer, Berlin, 2002), pp. 109–116
6. M Silveira, JC Nascimento, JS Marques, ARS Marcal, T Mendonca, S Yamauchi, J Maeda, J Rozeira, Comparison of segmentation methods for melanoma diagnosis in dermoscopy images. *IEEE J. Selected Topics Signal Process.* **3**(1), 35–45 (2009)
7. H Castillejos, V Ponomaryov, L Nino-de-Rivera, V Golikov, Wavelet transform fuzzy algorithms for dermoscopic image segmentation. *Comput. Math. Methods Med.* **2012**, 578721 (2012)
8. B Choi, B Chung, J Ryou, in *Proceedings of the International Conference on Computer Sciences and Convergence Information Technology (ICCIT)*. Adult image detection using Bayesian decision rule weighted by SVM probability (Seoul, Korea, 2009), pp. 659–662
9. M Kawulok, J Kawulok, J Nalepa, Spatial-based skin detection using discriminative skin-presence features. *Pattern Recogn. Lett.* **41**, 3–13 (2014)
10. R Khan, A Hanbury, J Stöttinger, A Bais, Color based skin classification. *Pattern Recogn. Lett.* **33**(2), 157–163 (2012)
11. M Kawulok, J Kawulok, J Nalepa, M Papiez, in *Proceedings of the IEEE International Conference on Image Processing (ICIP)*. Skin detection using spatial analysis with adaptive seed (Melbourne, Australia, 2013), pp. 3720–3724
12. J Kovac, P Peer, F Solina, Human skin color clustering for face detection. *EUROCON* **2**, 144–148 (2003)
13. J-C Terrillon, M David, S Akamatsu, in *Proceedings of the International Conference on Automatic Face and Gesture Recognition*. Automatic detection of human faces in natural scene images by use of a skin color model and of invariant moments (Nara, Japan, 1998), pp. 112–117
14. A Cheddad, J Condell, K Curran, P Mc Kevitt, A skin tone detection algorithm for an adaptive approach to steganography. *Signal Process.* **89**(12), 2465–2478 (2009)
15. Y-H Chen, K-T Hu, S-J Ruan, Statistical skin color detection method without color transformation for real-time surveillance systems. *Eng. Appl. Artif. Intell.* **25**(7), 1331–1337 (2012)
16. MJ Jones, JM Rehg, Statistical color models with application to skin detection. *Int. J. Comput. Vis.* **46**, 81–96 (2002)
17. SL Phung, A Bouzerdoum, D Chai, Skin segmentation using color pixel classification: analysis and comparison. *IEEE Trans. Pattern Anal. Mach. Intell.* **27**(1), 148–154 (2005)
18. T Chaira, AK Ray, Fuzzy approach for color region extraction. *Pattern Recognit. Lett.* **24**(12), 1943–1950 (2003)
19. H Greenspan, J Goldberger, I Eshet, Mixture model for face-color modeling and segmentation. *Pattern Recognit. Lett.* **22**, 1525–1536 (2001)
20. TS Caetano, SD Olabarriaga, DAC Barone, Do mixture models in chromaticity space improve skin detection? *Pattern Recognit.* **36**, 3019–3021 (2003)
21. SL Phung, A Bouzerdoum, D Chai, in *Proceedings of the International Conference on Image Processing (ICIP)*, vol. 1. A novel skin color model in YCbCr color space and its application to human face detection, (2002), pp. 289–292
22. M-J Seow, D Valaparla, VK Asari, in *Proceedings of the Applied Imagery Pattern Recognition Workshop*. Neural network based skin color model for face detection, (2003), pp. 141–145
23. KK Bhoyar, OG Kakde, Skin color detection model using neural networks and its performance evaluation. *J. Comput. Sci.* **6**(9), 963–968 (2010)
24. M Kawulok, J Nalepa, in *Lecture Notes in Computer Science: Structural, Syntactic, and Statistical Pattern Recognition*, vol. 7626, ed. by G Gimel'farb, E Hancock, A Imaiya, A Kuijper, M Kudo, S Omachi, T Windeatt, and K Yamada. Support vector machines training data selection using a genetic algorithm (Springer, New York, 2012), pp. 557–565
25. J Han, G Awad, A Sutherland, H Wu, in *Proceedings of the IEEE International Conference on Automatic Face and Gesture Recognition*. Automatic skin segmentation for gesture recognition combining region and support vector machine active learning (IEEE Computer Society, Washington D.C., 2006), pp. 237–242
26. ME Celebi, HA Kingravi, H Iyatomi, Y Alp Aslandogan, WV Stoecker, RH Moss, JM Malters, JM Grichnik, AA Marghoob, HS Rabinovitz, SW Menzies, Border detection in dermoscopy images using statistical region merging. *Skin Res. Tech.* **14**(3), 347–353 (2008)
27. ME Celebi, H Iyatomi, G Schaefer, WV Stoecker, Lesion border detection in dermoscopy images. *Comput. Med. Imag. Graph.* **33**(2), 148–153 (2009)
28. Q Abbas, ME Celebi, I Fondón García, M Rashid, Lesion border detection in dermoscopy images using dynamic programming. *Skin Res. Tech.* **17**(1), 91–100 (2011)
29. J Jaworek-Korjakowska, R Tadeusiewicz, in *Proceedings of the IEEE International Conference on Image Processing (ICIP)*. Assessment of dots and globules in dermoscopic color images as one of the 7-point check list criteria (Melbourne, Australia, 2013), pp. 1456–1460

30. G Yang, H Li, L Zhang, Y Cao, in *Proceeding of the International Conference on Communications and Intelligence Information Security (ICCIIS)*. Research on a skin color detection algorithm based on self-adaptive skin color model, (2010), pp. 266–270
31. M-J Zhang, W Gao, in *Proceedings of the IEEE International Conference on Image Processing (ICIP)*, vol. 2. An adaptive skin color detection algorithm with confusing backgrounds elimination, (2005), pp. 390–393
32. H-M Sun, Skin detection for single images using dynamic skin color modeling. *Pattern Recogn.* **43**(4), 1413–1420 (2010)
33. F Dadgostar, A Sarrafzadeh, An adaptive real-time skin detector based on hue thresholding: a comparison on two motion tracking methods. *Pattern Recogn. Lett.* **27**(12), 1342–1352 (2006)
34. P Yogarajah, J Condell, K Curran, P McKeivitt, A Cheddad, A dynamic threshold approach for skin segmentation in color images. *Int. J. Biometrics.* **4**(1), 38–55 (2012)
35. M Kawulok, in *Lecture Notes in Computer Science: Image and Signal Processing*, vol. 5099, ed. by A Elmoataz, O Lezoray, F Nouboud, and D Mammass. Dynamic skin detection in color images for sign language recognition (Springer, New York, 2008), pp. 112–119
36. AA Argyros, MIA Lourakis, in *Lecture Notes in Computer Science: Computer Vision - ECCV 2004*, vol. 3023, ed. by T Pajdla, J Matas. Real-time tracking of multiple skin-colored objects with a possibly moving camera (Springer, New York, 2004), pp. 368–379
37. J Fritsch, S Lang, M Kleinehagenbrock, GA Fink, G Sagerer, in *Proceedings of the IEEE International Workshop on Robot and Human Interactive Communication*. Improving adaptive skin color segmentation by incorporating results from face detection, (2002), pp. 337–343
38. M Soriano, B Martinkauppi, S Huovinen, M Laaksonen, in *Proceedings of the IEEE International Conference on Pattern Recognition*, vol. 1. Skin detection in video under changing illumination conditions, (2000), pp. 839–842
39. J Lichtenauer, MJT Reinders, EA Hendriks, in *Proceedings of the International Conference on Computer Vision Theory and Applications*, vol. 1. A self-calibrating chrominance model applied to skin color detection, (2007), pp. 115–120
40. P Yogarajah, J Condell, K Curran, A Cheddad, P McKeivitt, in *Proceedings of the IEEE International Conference on Image Processing (ICIP)*. A dynamic threshold approach for skin segmentation in color images (Hong Kong, 2010), pp. 2225–2228
41. Q Zhu, K-T Cheng, C-T Wu, Y-L Wu, in *Proceedings of the IEEE International Conference on Automatic Face and Gesture Recognition*. Adaptive learning of an accurate skin-color model, (2004), pp. 37–42
42. X Wang, X Zhang, J Yao, in *Proceedings of the International Conference on Mechatronic Science, Electric Engineering and Computer (MEC)*. Skin color detection under complex background, (2011), pp. 1985–1988
43. AY Taqa, HA Jalab, Increasing the reliability of skin detectors. *Sci. Res. Essays* **5**(17), 2480–2490 (2010)
44. B Zafarifar, A Martiniere, PHN de With, in *Proceedings of the International Conference on Consumer Electronics (ICCE)*. Improved skin segmentation for tv image enhancement, using color and texture features, (2010), pp. 373–374
45. P Ng, C-M Pun, in *International Conference on Computational Intelligence, Communication Systems and Networks (CICSyN)*. Skin color segmentation by texture feature extraction and K-mean clustering, (2011), pp. 213–218
46. DA Forsyth, MM Fleck, Automatic detection of human nudes. *Int. J. Comput. Vis.* **32**, 63–77 (1999)
47. A Conci, E Nunes, JJ Pantrigo, Á Sánchez, in *Proceedings of the International Conference on Enterprise Information Systems (ICEIS)*. Comparing color and texture-based algorithms for human skin detection, (2008), pp. 166–173
48. M Fotouhi, MH Rohban, S Kasaei, in *Proceedings of the International Conference on Digital Telecommunications (ICDT)*. Skin detection using contourlet-based texture analysis, (2009), pp. 59–64
49. AA Abin, M Fotouhi, S Kasaei, A new dynamic cellular learning automata-based skin detector. *Multimed. Syst.* **15**(5), 309–323 (2009)
50. M Kawulok, in *Lecture Notes in Computer Science: Pattern Recognition*, vol. 7329, ed. by JA Carrasco-Ochoa, JF Martinez-Trinidad, JA Olvera Lopez, and KL Boyer. Texture analysis for skin probability maps refinement (Springer, New York, 2012), pp. 75–84
51. MG Bello, A combined Markov random field and wave-packet transform-based approach for image segmentation. *IEEE Trans. Image Process.* **3**(6), 834–846 (1994)
52. S Alpert, M Galun, R Basri, A Brandt, in *Proceedings of the IEEE Conference on Computer Vision and Pattern Recognition (CVPR)*. Image segmentation by probabilistic bottom-up aggregation and cue integration, (2007), pp. 1–8
53. X-P Zhang, MD Desai, Segmentation of bright targets using wavelets and adaptive thresholding. *IEEE Trans. Image Process.* **10**(7), 1020–1030 (2001)
54. VI Ponomaryov, H Castillejos, R Peralta-Fabi, in *Proceedings of the SPIE, Real-Time Image and Video Processing*, vol. 8437. Image segmentation in wavelet transform space implemented on DSP, (2012). <http://proceedings.spiedigitallibrary.org/proceeding.aspx?articleid=1316590>
55. H Baltzakis, M Pateraki, P Trahanias, Visual tracking of hands, faces and facial features of multiple persons. *Mach. Vis. Appl.* **23**, 1141–1157 (2012)
56. K Chenaoua, A Bouridane, in *Proceedings of the IEEE International Conference on Image Processing (ICIP)*. Skin detection using a Markov random field and a new color space, (2006), pp. 2673–2676
57. J Ruiz-del-Solar, R Verschae, in *Proceedings of the IEEE International Conference on Automatic Face and Gesture Recognition*. Skin detection using neighborhood information, (2004), pp. 463–468
58. M Kawulok, Energy-based blob analysis for improving precision of skin segmentation. *Multimed. Tool Appl.* **49**(3), 463–481 (2010)
59. M Kawulok, in *Proceedings of the IEEE International Conference on Automatic Face and Gesture Recognition*. Fast propagation-based skin regions segmentation in color images (Shanghai, China, 2013), pp. 1–7
60. M Kawulok, in *Lecture Notes in Computer Science: Computer Vision and Graphics*, vol. 7594, ed. by L Bolc, R Tadeusiewicz, L Chmielewski, and K Wojciechowski. Skin detection using color and distance transform (Springer, New York, 2012), pp. 449–456
61. Z Jiang, M Yao, W Jiang, in *Proceedings of the International Conference on Fuzzy Systems and Knowledge Discovery (FSKD)*, vol. 3. Skin detection using color, texture and space information, (2007), pp. 366–370
62. R Khan, A Hanbury, R Sablatnig, J Stoeettinger, FA Khan, FA Khan, Systematic skin segmentation: merging spatial and non-spatial data. *Multimed. Tool Appl.* **69**(3), 717–741 (2014)
63. L Ikonen, P Toivanen, Shortest routes on varying height surfaces using gray-level distance transforms. *Image Vis. Comput.* **23**(2), 133–141 (2005)
64. T Ojala, M Pietikainen, T Maenpaa, Multiresolution gray-scale and rotation invariant texture classification with local binary patterns. *IEEE Trans. Pattern Anal. Mach. Intell.* **24**(7), 971–987 (2002)
65. SL Phung, D Chai, A Bouzerdoum, in *Proceedings of the IEEE International Conference on Acoustics, Speech, and Signal Processing (ICASSP)*. Adaptive skin segmentation in color images, (2003), pp. 353–356
66. M Kawulok, J Szymankiewicz, Precise multi-level face detector for advanced analysis of facial images. *IET Image Process.* **6**(2), 95–103 (2012)
67. T Fawcett, An introduction to ROC analysis. *Pattern Recogn. Lett.* **27**(8), 861–874 (2006)
68. J Davis, M Goadrich, in *Proceedings of the International Conference on Machine Learning*. The relationship between Precision-Recall and ROC curves, (2006), pp. 233–240

doi:10.1186/1687-6180-2014-170

Cite this article as: Kawulok et al.: Self-adaptive algorithm for segmenting skin regions. *EURASIP Journal on Advances in Signal Processing* 2014 **2014**:170.

Submit your manuscript to a SpringerOpen® journal and benefit from:

- Convenient online submission
- Rigorous peer review
- Immediate publication on acceptance
- Open access: articles freely available online
- High visibility within the field
- Retaining the copyright to your article

Submit your next manuscript at ► [springeropen.com](http://springeropen.com)